Wave Motion 88 (2019) 85–105

Contents lists available at ScienceDirect

Wave Motion

journal homepage: www.elsevier.com/locate/wamot

Inverse metamaterial design for controlling band gaps in scalar wave problems

Heedong Goh [a], Loukas F. Kallivokas [a,b,*]

[a] Department of Civil, Architectural and Environmental Engineering, The University of Texas at Austin, Austin, TX, USA
[b] The Institute for Computational Engineering & Sciences, The University of Texas at Austin, Austin, TX, USA

HIGHLIGHTS

- A systematic inverse medium-based approach for band-gap design in metamaterials.
- Identification of band gaps with a simple scalar metric characterizing the unit-cell.
- Inverse material design for user-defined omni-directional band gaps in 2D.

ARTICLE INFO

Article history:
Received 28 November 2017
Received in revised form 8 January 2019
Accepted 11 February 2019
Available online 15 February 2019

Keywords:
Band gap
Metamaterial
Inverse design
Dispersion-constrained optimization
Wave control

ABSTRACT

We are concerned with the design of metamaterials capable of exhibiting a user-defined frequency band gap in periodic media supporting scalar waves. We cast the metamaterial design problem as an inverse medium problem, and seek to reveal the properties of the metamaterial unit cell that would enforce the gap. To drive the inversion, we use a scalar objective functional – the negativity of a discriminant of the coefficients of a quadratic wavenumber eigenvalue problem – that defines uniquely the evanescent state associated with the gap. We use the medium's dispersion characteristics to side-impose the underlying wave physics in the objective functional, and demonstrate the proposed inverse metamaterial design with numerical examples in both the frequency and time domains for the scalar wave case in one and two dimensions. The approach is systematic and can be generalized to the vector wave case, since the associated eigenvalue problem remains Hermitian.

1. Introduction

The need to design materials capable of exhibiting band gaps is driven, with increasing intensity, by applications in various engineering fields: whereas electronic band gaps have long been central to developments in the semiconductor industry [1], applications involving photonic and phononic crystals are currently driving novel applications in sensing and imaging [2,3]. A photonic crystal and a phononic crystal are spatially periodic composite structures capable of exhibiting electromagnetic or acoustic band gaps, respectively. In this context, a band gap is a frequency range where the propagation of waves is arrested. The crystal's spatially periodic structure is realized by assemblies of unit cells; typically, each unit cell is itself heterogeneous, with spatially varying optical or acoustic properties. Whereas the unit cell's constituent materials are real, the crystal's homogenized properties may assume non-physical values, thus granting metamaterial status to the crystal. Depending on the type of crystal, the wave type to be arrested in a band gap is different: de Broglie waves in the "electronic"

* Corresponding author at: Department of Civil, Architectural and Environmental Engineering, The University of Texas at Austin, Austin, TX, USA.
E-mail addresses: heedong.goh@utexas.edu (H. Goh), loukas@mail.utexas.edu (L.F. Kallivokas).

https://doi.org/10.1016/j.wavemoti.2019.02.001
0165-2125/

crystal case, electromagnetic and sound waves, in the photonic and phononic crystal cases, respectively. Band-gap behavior similar to that exhibited in photonic or phononic crystals is also possible for elastic waves in elastic metamaterials. Whereas the one-dimensional elastic band-cap case is very similar to the photonic and phononic crystal cases, designing materials to exhibit band gaps in higher dimensions remains a challenge due to the presence of multiple directions and of different wave types that travel at different velocities (e.g., shear and compressional waves).

Most of the early studies on band-gap materials were the purview of solid-state physics (the electronic band gap) [1,4]. The photonic crystal case, and more recently the phononic case, have seen considerable development, especially since technological challenges in the fabrication of the crystals were overcome [5,6]. More generally, the interest in understanding how waves interact with periodic structures possibly predates all the aforementioned developments and it seems to have originated in studies of the behavior of elastic or stress waves in periodic structures [7]. Irrespective of the underlying physics, the inverse design problem, or equivalently, the question of what should the unit cell be made of in order to deliver a prescribed or desired band gap has not been systematically addressed, relying mostly on *ad hoc* approaches, with very few exceptions [8–12].

In this paper, we are concerned with devising one such systematic approach for the material design of a metamaterial unit cell, when given a target design band gap. Herein, we focus exclusively on the scalar wave problem, which is common to acoustics, particular polarization cases in electromagnetics (e.g., TE or TM cases), and elastodynamics (e.g., SH case). Since the goal is to construct the spatial distribution of material properties driven by given data (or a sought performance outcome), the problem belongs to the class of inverse medium problems encountered in various other fields (e.g., geophysics): we thus borrow from our own past developments in the treatment of inverse medium problems using PDE-constrained optimization [13,14], with suitable modifications to accommodate the band-gap objective. Specifically, we show that the negativity of the discriminant of the coefficients of the problem's eigenvalue problem (cast in terms of the wavenumber) is sufficiently unique in delineating the band gap, and thus is a good choice to base the objective functional on. To form the Lagrangian, instead of side-imposing the governing PDE, we augment the objective functional with the side imposition of the problem's dispersion characteristics, or equivalently, the eigenvalue problem. Following the satisfaction of the first-order optimality conditions, the properties of the unit cell are obtained, leading to a metamaterial exhibiting the target band gap. We demonstrate the methodology with numerical results, leading to unit cell designs with either piecewise constant properties, or made of functionally-graded materials, in one and two spatial dimensions.

2. Preliminaries

To justify the particular choice of the objective functional that would drive the inversion for the metamaterial unit cell, we discuss first the dynamics of a periodic structure that lead to an eigenvalue problem for the unit cell. The eigenvalue problem characterizes fully the dispersion behavior and the frequency band structure of the metamaterial.

2.1. Bloch theorem and Bloch boundary condition

Consider the one-dimensional elastic metamaterial shown in Fig. 1, consisting of one-dimensional unit cells. In the frequency domain, the wave propagation within the metamaterial is governed by the one-dimensional scalar Helmholtz equation:

$$\frac{\partial}{\partial x}\left[\mu(x)\frac{\partial}{\partial x}U(x)\right]+\omega^2\rho(x)\,U(x)=0,\quad \forall x\in\mathbb{R}, \tag{1}$$

where ω is a temporal frequency and the two material properties μ (elastic modulus) and ρ (mass density) are periodic with periodicity p, i.e., $\mu(x+p)=\mu(x)$, and $\rho(x+p)=\rho(x)$; consequently, the Helmholtz operator in (1) is periodic. Then, by virtue of the Bloch theorem [4], the wavefunctions $U(x)$ that are solutions to (1) are Bloch waves, i.e.:

$$U(x)=e^{\mathrm{i}kx}u(x), \tag{2}$$

where $u(x+p)=u(x)\ \forall x$, and k is the (Bloch) wavenumber. Expression (2) leads also to the Bloch boundary condition:

$$U(x+p)=e^{\mathrm{i}kp}U(x), \tag{3}$$

which permits consideration of the unit cell only.

We note that (1) is equally applicable to the acoustic, electromagnetic (polarized cases), and elastic cases, with different ascription of physical meaning to the material properties ρ and μ [15].

2.2. Eigenvalue problems and band structures

Next, we are interested in deriving the unit cell's eigenvalue problem. Since we intend to use finite elements for the numerical treatment of the inverse material design problem, the eigenvalue problem is derived in a weak or weighted-residual sense: we multiply (1) by a test function $V(x)$, where $V(x)=e^{\mathrm{i}\bar{k}x}v(x)$, with $v(0)=v(p)$, and a bar $\overline{(\cdot)}$ over a variable denotes complex-conjugation of the subtended quantity. Then:

$$0=\int_0^p \overline{V}\left[\frac{\partial}{\partial x}\left(\mu\frac{\partial U}{\partial x}\right)+\omega^2\rho\,U\right]dx$$

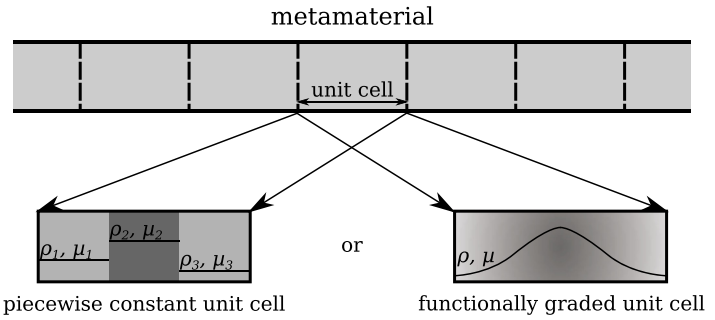

Fig. 1. Typical one-dimensional metamaterial.

$$
\begin{aligned}
&= \overline{V}\mu \frac{\partial U}{\partial x}\Big|_{x=0}^{x=p} - \int_0^p \left[\frac{\partial \overline{V}}{\partial x}\mu \frac{\partial U}{\partial x} - \overline{V}\omega^2 \rho\, U \right] dx \\
&= \overline{V}\mu \left(e^{\mathrm{i}kx}\mathrm{i}ku + e^{\mathrm{i}kx}\frac{\partial u}{\partial x} \right)\Big|_{x=0}^{x=p} \\
&\quad - \int_0^p \left[\frac{\partial \overline{V}}{\partial x}\mu \left(e^{\mathrm{i}kx}\mathrm{i}ku + e^{\mathrm{i}kx}\frac{\partial u}{\partial x} \right) - \overline{V}\omega^2 \rho\, e^{\mathrm{i}kx} u \right] dx. \qquad (4)
\end{aligned}
$$

Eq. (4) is a Hermitian form, which yields the Bloch eigenvalue problem [16,17] in a weak sense:

$$
0 = \int_0^p \left[\left(-\mathrm{i}k\overline{v} + \frac{\partial \overline{v}}{\partial x} \right) \mu \left(\mathrm{i}ku + \frac{\partial u}{\partial x} \right) - \overline{v}\omega^2 \rho u \right] dx. \qquad (5)
$$

In the above u, $v \in \mathcal{V}$, where $\mathcal{V}$ is defined as:

$$
\mathcal{V} = \left\{ u \in H^1(0,p)\,|\, , u(0) = u(p) \right\}. \qquad (6)
$$

There are two paths one can follow to obtain the band structure from the eigenvalue problem: for a given wavenumber k, one can solve for ω^2, which gives rise to a linear eigenvalue problem, or, alternatively, one can solve for the wavenumber k for a given ω, which gives rise to a quadratic eigenvalue problem.

A classical band structure, as that shown in Fig. 2(a), results from the solution of the linear eigenvalue problem: in the figure, $\hat{\omega} = \omega p/c_a$ and $\hat{k} = kp/\pi$ is normalized frequency and wavenumber, respectively, and c_a denotes an average wave velocity. The bands are symmetric about the origin of the Brillouin zone[1] Γ, and they are periodic. Thus, the bands between Γ and the center of the face X contain all the information of the band structure. We note that to solve the linear eigenvalue problem, we use real-valued wavenumbers k, and since the associated forms are Hermitian, ω^2 is always real-valued. Therefore, the resulting classical band structure can express propagating states only, with the evanescent states corresponding to band gaps that are only indirectly recoverable: the shadowed region in Fig. 2(a) corresponds to a no-solution condition for ω. Due to the above indirect definition of the band gap, the linear eigenvalue problem does not appear to be the best driver for the inverse problem. By contrast, the quadratic eigenvalue problem offers a direct definition of the evanescent state/band gap, as is discussed next. We note that, in the quadratic eigenvalue problem, for a given (real) ω, we solve for k, which is, in general, complex. To illustrate, we rearrange the weak form (5) to yield the quadratic eigenvalue problem:

Given $\omega \in \mathbb{R}$, find $k \in \mathbb{C}$ and $u \in \mathcal{V} \setminus \{0\}$ such that:

$$
0 = a_0(v,u) + k a_1(v,u) + k^2 a_2(v,u) \equiv P(k)(v,u), \quad \forall v \in \mathcal{V} \qquad (7)
$$

where

$$
a_0(v,u) = \int_0^p \left(\frac{\partial \overline{v}}{\partial x}\mu \frac{\partial u}{\partial x} - \omega^2 \overline{v}\rho u \right) dx, \qquad (8a)
$$

$$
a_1(v,u) = \int_0^p \mathrm{i} \left(\frac{\partial \overline{v}}{\partial x}\mu u - \overline{v}\mu \frac{\partial u}{\partial x} \right) dx, \text{ and} \qquad (8b)
$$

$$
a_2(v,u) = \int_0^p \overline{v}\mu u dx. \qquad (8c)
$$

[1] The Brillouin zone is a unit cell in the spatial Fourier transform of the periodic domain. The first Brillouin zone contains the origin $\hat{k} = 0$, which is denoted by Γ. The boundary of the first Brillouin zone $\hat{k} = 1$, or the center of the face, is denoted by X.

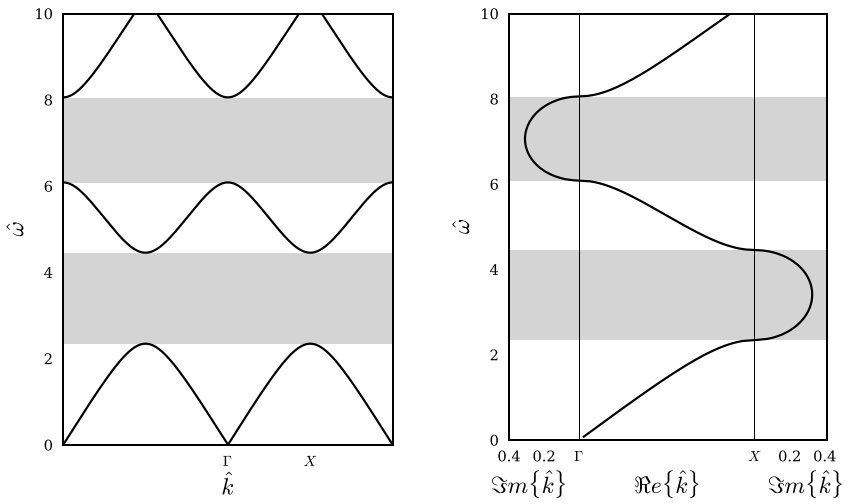

(a) Classical band structure **(b)** Complex band structure

Fig. 2. Band structures: (a) The classical band structure plotted using the periodic zone scheme. (b) The complex band structure plotted using the reduced zone scheme; $\Re e\{\hat{k}\}$ is in the middle panel, the non-zero $\Im m\{\hat{k}\}$ for $\Re e\{\hat{k}\} = 0$ is in the left panel, and the non-zero $\Im m\{\hat{k}\}$ for $\Re e\{\hat{k}\} = 1$ is in the right panel. Band gaps correspond to the shadow zones.

Fig. 2(b) depicts the band structure resulting from the quadratic eigenvalue problem, where, because of the symmetry and the periodicity, the band structure is plotted only between Γ and X. We note that the band gaps correspond to the regions where $\Im m\{\hat{k}\}$ is non-zero; in particular, the left panel corresponds to $\Re e\{\hat{k}\} = 0$, whereas the right panel corresponds to $\Re e\{\hat{k}\} = 1$. Clearly, whether recovered by the linear or the quadratic eigenvalue problems, the band gaps coincide, as shown in Figs. 2(a) and 2(b), respectively. However, the quadratic eigenvalue problem offers a sharper criterion for establishing the band gap than its linear counterpart, as it can be readily seen in Fig. 2(b): the criterion is a non-zero imaginary wavenumber part, which will be further exploited in defining the objective functional.

2.3. Eigenvalue problem discriminant

We revisit the eigenvalue problem (7) and replace the test function v with the eigenfunction u: there results a simple quadratic equation in the wavenumber k, i.e.,

$$\begin{aligned} 0 =& P(k)(u,u) \\ =& a_0(u,u) + k a_1(u,u) + k^2 a_2(u,u) \\ =& c + bk + ak^2, \end{aligned} \tag{9}$$

where the coefficients $a = a_2(u,u)$, $b = a_1(u,u)$, and $c = a_0(u,u)$ are always real-valued because they are the products of Hermitian forms operating on the same function. Then, the solutions of (9) are obtained by the quadratic formula:

$$k = \frac{-b \pm \sqrt{b^2 - 4ac}}{2a}, \tag{10}$$

where the discriminant $\mathcal{D}$ is defined as:

$$\mathcal{D} = b^2 - 4ac. \tag{11}$$

The negativity of the discriminant (11) ensures a non-zero imaginary part for the wavenumber: the latter was associated in the previous section with the presence of a band gap. Fig. 3 depicts the discriminant as a function of the temporal frequency ω, side-by-side with the band structure. Clearly, positive discriminants are associated with propagating states, while negative discriminants appear at evanescent states.

Thus, in summary, band gaps are equivalently characterized by either wavenumbers with non-zero imaginary parts or by negative discriminants, for a given temporal frequency. Either of the two band-gap indicators ($\Im m\{k\} \neq 0$ or $\mathcal{D} < 0$) could be used to drive the inverse metamaterial design: however, only the discriminant-based indicator allows for differentiable objective functionals.

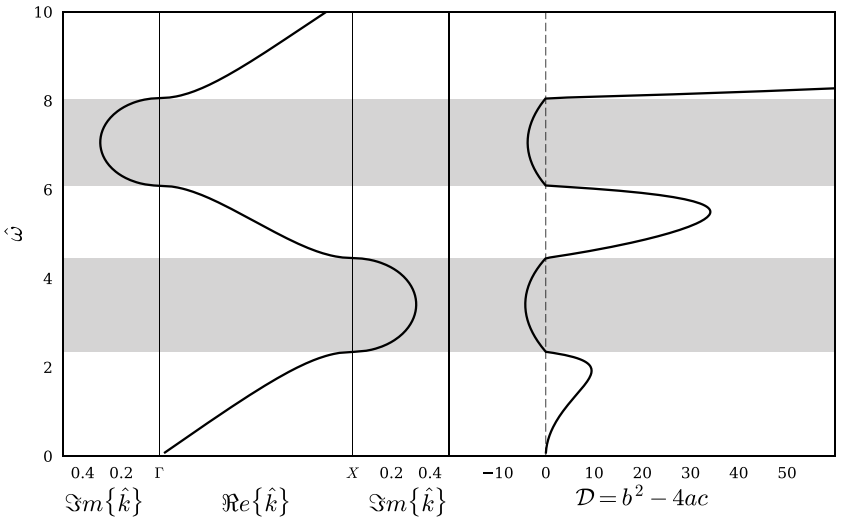

Fig. 3. A typical band structure (left) and the discriminant of the associated quadratic eigenvalue problem (right): the discriminants are real-valued and are smoothly varying over the frequency range. Negative discriminants correspond to band gaps (shaded zones).

3. Inverse metamaterial design in 1D

3.1. Discriminant-based objective functional

Suppose we want to design a material that exhibits a band gap at frequencies between ω_s and ω_f. Then, the design goal in terms of the discriminant becomes:
Find ρ and μ such that

$$\mathcal{D} < 0, \ \ \omega \in (\omega_s, \omega_f), \tag{12}$$

or, by restating the above inequality problem as a minimization problem:
Given $\omega_i \in (\omega_s, \omega_f)$, find ρ and μ such that:

$$\min D\left[\rho, \mu, u\right]. \tag{13}$$

The target band-gap interval is discretized into N frequencies $\omega^{(i)}$, with $i = 1, 2, \ldots, N$. Then, given $\omega^{(i)} \in (\omega_s, \omega_f)$, the objective functional can be written as:

$$D\left[\rho, \mu, u\right] = \sum_{i}^{N} \mathcal{D}_0^{(i)}\left[\rho, \mu, u_0^{(i)}\right], \ \text{where} \tag{14a}$$

$$\mathcal{D}_0^{(i)}\left[\rho, \mu, u_0^{(i)}\right] = a_1\left(u_0^{(i)}, u_0^{(i)}\right) a_1\left(u_0^{(i)}, u_0^{(i)}\right) - 4a_2\left(u_0^{(i)}, u_0^{(i)}\right) a_0\left(u_0^{(i)}, u_0^{(i)}\right). \tag{14b}$$

In the above, we use $u_0^{(i)}$ to denote the fundamental eigenfunction at each frequency $\omega^{(i)}$, and u to represent the set of all $u_0^{(i)}$ across the target band gap. Similarly, $\mathcal{D}_0^{(i)}$ denotes the ith discriminant of the fundamental mode eigenvalue problem. In one spatial dimension, the objective functional consists of the sum of the fundamental-mode discriminants $\mathcal{D}_0^{(i)}$ at the target frequencies $\omega^{(i)}$, and was proven sufficient for driving the inverse design. However, the fundamental mode may not be sufficient for waves in higher spatial dimensions, as is discussed in Section 4, where suitable augmentations are presented.

3.2. The Lagrangian and the dispersion constraint

Resolution of the minimization problem (13) requires the direct sensitivity analysis of the objective functional D. Alternatively, an adjoint method could be enlisted to compute the gradient that drives the material parameter updates during the inversion process. To this end, the objective functional D could be augmented by the side imposition of a constraint — typically, a mathematical description of the underlying wave physics. Such an often-used constraint is the problem's partial differential equation (e.g., [13,14]); here we opt to instead use the associated eigenvalue problem, effectively constraining the minimization by the dispersive properties of the target medium (e.g., [18,19]). The resulting Lagrangian functional becomes:

$$L\left[\rho, \mu, u, k, v, \xi\right] = D\left[\rho, \mu, u\right] + E\left[\rho, \mu, u, k, v, \xi\right], \tag{15}$$

where the constraint $E[\rho, \mu, u, k, v, \xi]$ is defined as:

$$E[\rho, \mu, u, k, v, \xi] = \sum_i^N \Re e\left\{P\left(k_0^{(i)}\right)\left(v_0^{(i)}, u_0^{(i)}\right)\right\} + \sum_i^N \frac{\xi_0^{(i)}}{2}\left[a_2\left(u_0^{(i)}, u_0^{(i)}\right) - 1\right]. \tag{16}$$

In (16), $u_0^{(i)}$ is the fundamental mode eigenfunction (or the eigenfunction that is associated with the smallest eigenvalue), $k_0^{(i)}$ is the corresponding fundamental eigenvalue, $v_0^{(i)}$ is an adjoint eigenfunction, and $\xi_0^{(i)}$ is an adjoint variable at each frequency $\omega^{(i)}$ (the sets of all $k_0^{(i)}$, $\xi_0^{(i)}$, and $v_0^{(i)}$ are denoted by k, ξ, and v, respectively). Thus, the first term in (16) is the eigenvalue problem (7); without loss of generality, we impose the real part of the eigenvalue problem to ensure its derivative is real-valued. The second term in (16) is the orthonormality condition that would guarantee a unique solution for the eigenvectors. With the above definition for the Lagrangian, the inverse design problem (13) is replaced by:

$$\min L[\rho, \mu, u, k, v, \xi]. \tag{17}$$

The minimization of the Lagrangian L would ensure the simultaneous minimization of the objective functional D (band-gap goal), and the satisfaction of the eigenvalue problem.

3.3. Optimality conditions

Next, we seek a stationary point of the Lagrangian (15) by requiring the satisfaction of the first-order optimality conditions. Accordingly, the first (Gâteaux) derivatives of L with respect to the state variables, to the adjoint variables, and to the (unknown) design material variables, are forced to vanish. The derivatives with respect to the adjoint variables lead to the state eigenvalue problem, whereas the derivatives with respect to the state variables lead to the adjoint eigenvalue problem. The derivatives with respect to the design variables lead to a control problem, from which we obtain the gradient of L for given trial designs of ρ and μ. The definitions of the derivatives are given in Appendix; here, we provide the final form of the optimality conditions:

1. **State eigenvalue problem**
   Given trials ρ and μ, find $k_0^{(i)} \in \mathbb{C}$ and $u_0^{(i)} \in \mathcal{V} \setminus \{0\}$ such that

$$0 = P\left(k_0^{(i)}\right)\left(\tilde{v}_0^{(i)}, u_0^{(i)}\right) \quad \forall \tilde{v}_0^{(i)} \in \mathcal{V} \tag{18a}$$

$$0 = \frac{\tilde{\xi}_0^{(i)}}{2}\left[a_2\left(u_0^{(i)}, u_0^{(i)}\right) - 1\right] \quad \forall \tilde{\xi}_0^{(i)} \in \mathbb{R}. \tag{18b}$$

2. **Adjoint eigenvalue problem**
   Given trials ρ, μ, and state variables $k_0^{(i)}$ and $u_0^{(i)}$, find $\xi_0^{(i)} \in \mathbb{R}$ and $v_0^{(i)} \in \mathcal{V}$ such that

$$\begin{aligned} 0 =& P\left(k_0^{(i)}\right)\left(v_0^{(i)}, \tilde{u}_0^{(i)}\right) + \xi_0^{(i)} a_2\left(u_0^{(i)}, \tilde{u}_0^{(i)}\right) + 4a_1\left(u_0^{(i)}, u_0^{(i)}\right) a_1\left(u_0^{(i)}, \tilde{u}_0^{(i)}\right) \\ & - 8a_2\left(u_0^{(i)}, u_0^{(i)}\right) a_0\left(u_0^{(i)}, \tilde{u}_0^{(i)}\right) - 8a_0\left(u_0^{(i)}, u_0^{(i)}\right) a_2\left(u_0^{(i)}, \tilde{u}_0^{(i)}\right) \quad \forall \tilde{u}_0^{(i)} \in \mathcal{V} \end{aligned} \tag{19a}$$

$$0 = \tilde{k}_0^{(i)} a_1\left(v_0^{(i)}, u_0^{(i)}\right) + 2\tilde{k}_0^{(i)} k_0^{(i)} a_2\left(v_0^{(i)}, u_0^{(i)}\right) \quad \forall \tilde{k}_0^{(i)} \in \mathbb{C}. \tag{19b}$$

3. **Gradient of L**
   Given trials ρ, μ, state variables $k_0^{(i)}$ and $u_0^{(i)}$, adjoint variables $\xi_0^{(i)}$ and $v_0^{(i)}$, find $g_\rho \in \mathcal{S}$ and $g_\mu \in \mathcal{S}$ such that

$$\int_0^p \tilde{\rho}\, g_\rho dx = \sum_i^N \Re e\left\{4a_2\left(u_0^{(i)}, u_0^{(i)}\right)\int_0^p \overline{u}_0^{(i)} \omega^2 \tilde{\rho}\, u_0^{(i)} dx\right\} - \sum_i^N \Re e\left\{\int_0^p \overline{v}_0^{(i)} \omega^2 \tilde{\rho}\, u_0^{(i)} dx\right\} \quad \forall \tilde{\rho} \in \mathcal{S} \tag{20a}$$

$$\begin{aligned} \int_0^p \tilde{\mu}\, g_\mu dx =& \sum_i^N \Re e\left\{2a_1\left(u_0^{(i)}, u_0^{(i)}\right)\int_0^p \mathrm{i}\left(\frac{\partial \overline{u}_0^{(i)}}{\partial x}\tilde{\mu}\, u_0^{(i)} - \overline{u}_0^{(i)}\tilde{\mu}\frac{\partial u_0^{(i)}}{\partial x}\right) dx\right\} \\ & - \sum_i^N \Re e\left\{4a_2\left(u_0^{(i)}, u_0^{(i)}\right)\int_0^p \frac{\partial \overline{u}_0^{(i)}}{\partial x}\tilde{\mu}\frac{\partial u_0^{(i)}}{\partial x} dx\right\} \\ & - \sum_i^N \Re e\left\{4a_0\left(u_0^{(i)}, u_0^{(i)}\right)\int_0^p \overline{u}_0^{(i)}\tilde{\mu}\, u_0^{(i)} dx\right\} \\ & + \sum_i^N \Re e\left\{k_0^{(i)}\int_0^p \mathrm{i}\left(\frac{\partial \overline{v}_0^{(i)}}{\partial x}\tilde{\mu}\, u_0^{(i)} - \overline{v}_0^{(i)}\tilde{\mu}\frac{\partial u_0^{(i)}}{\partial x}\right) dx\right\} + \sum_i^N \Re e\left\{\int_0^p \frac{\partial \overline{v}_0^{(i)}}{\partial x}\tilde{\mu}\frac{\partial u_0^{(i)}}{\partial x} dx\right\} \end{aligned}$$

$$+\sum_{i}^{N}\Re e\left\{\left(k_0^{(i)}\right)^2\int_0^p \overline{v}_0^{(i)}\tilde{\mu}\,u_0^{(i)}dx\right\}+\sum_{i}^{N}\Re e\left\{\frac{\xi_0^{(i)}}{2}\int_0^p \overline{u}_0^{(i)}\tilde{\mu}\,u_0^{(i)}dx\right\}\ \forall\tilde{\mu}\in\mathcal{S}, \tag{20b}$$

where

$$\mathcal{S}=\left\{u\in H^0(0,p)|u(0)=u(p)\right\}, \tag{21}$$

and g_ρ and g_μ are the Fréchet derivatives, or gradients, of L with respect to ρ and μ, respectively.

The search directions d_ρ and d_μ are constructed from the gradients g_ρ and g_μ, and the properties are then updated using any gradient-based scheme [20], e.g., steepest descent, conjugate gradient, etc. Given appropriate step sizes α_ρ and α_μ, the material profiles are updated by

$$\rho\leftarrow\rho+\alpha_\rho d_\rho, \tag{22a}$$

$$\mu\leftarrow\mu+\alpha_\mu d_\mu. \tag{22b}$$

The overall inversion algorithm, including the computational details for the search directions and the step sizes, is discussed in Section 3.5.

3.4. Band gap width control

An algorithm based on the described minimization of the Lagrangian would, in general, drive the discriminants for the band gap frequencies to negative territory, but would not necessarily stop from enlarging the band gap beyond the target regime, since no stopping criterion has been prescribed thus far. In this section, we discuss two approaches for limiting the band-gap width to the target size.

The simplest method is to implement a termination criterion by monitoring the negativity of the discriminants $\mathcal{D}_0^{(i)}$ at discrete frequencies $\omega^{(i)}$ within the target band gap. Let N_D denote the number of frequencies at which the discriminant becomes negative. Then, the inversion is terminated when

$$N_D\geq N, \tag{23}$$

i.e., when the number of frequencies at which the discriminant becomes negative exceeds the number of discrete frequencies within the target band gap.

Alternatively, one could replace the summations in (14) and (16) with conditional summations, per:

$$D[\rho,\mu,u]=\sum_{i|\mathcal{D}_0^{(i)}>0}^{N}\mathcal{D}_0^{(i)}\quad\text{and} \tag{24}$$

$$E[\rho,\mu,u,k,v,\xi]=\sum_{i|\mathcal{D}_0^{(i)}>0}^{N}\Re e\left\{P\left(k_0^{(i)}\right)\left(v_0^{(i)},u_0^{(i)}\right)\right\}+\sum_{i|\mathcal{D}_0^{(i)}>0}^{N}\frac{\xi_0^{(i)}}{2}\left[a_2\left(u_0^{(i)},u_0^{(i)}\right)-1\right]. \tag{25}$$

That is, the summations are carried only over the number of frequencies within the target band gap for which the associated (fundamental mode) discriminant is positive. By definition, the objective functional (24) has a lower bound (zero): the inversion process stops automatically when the discriminant becomes negative for every frequency $\omega^{(i)}$ in the target band gap. This second method is particularly useful for higher-dimensional problems, as it will be shown, where multiple modes and multiple directions are present.

In reporting numerical results, we used the first stopping criterion (23) for one-dimensional problems, and the second criterion (24)–(25) for two-dimensional problems.

3.5. Inversion process

We discuss next the inversion process that iteratively updates the unit cell properties to yield a metamaterial assembly capable of exhibiting a prescribed band gap. Other inverse design problems can be similarly accommodated depending on particular manufacturing constraints that may limit the range of considered material properties.

First, we choose initial guesses ρ_0 and μ_0 for the material properties ρ and μ. Then, using the trial material properties, the state eigenvalue problem (18) is solved to obtain the state variables $k_0^{(i)}$ and $u_0^{(i)}$. Then, using the state variables and the trial properties, the adjoint eigenvalue problem (19) is solved to obtain the adjoint variables $\xi_0^{(i)}$ and $v_0^{(i)}$. Next, armed with both the state and adjoint variables, the reduced gradient of the Lagrangian L is computed, per (20). The search directions for the material properties are obtained from the gradient of L using any gradient-based scheme; here, we opt for a nonlinear conjugate gradient method [20,21]. The step size is obtained using a backtracking algorithm [20], and, finally, the properties are updated using (22). The process is repeated until the inverted material satisfies the termination criterion (23). We also

stop the iterations when the backtracking algorithm fails to satisfy the sufficient-decrease condition; in such a case, we restart the inversion with different initial search length or initial guess for the material properties.

The most computationally-intensive parts of the inversion process are the state and the adjoint solutions, which contain N number of eigenvalue solutions, and N number of linear system solutions. However, the computation of the eigenvalue solution and the linear system solution for each frequency $\omega^{(i)}$ in the target band gap is independent from each other, and thus, the inversion process can be efficiently parallelized.

The details of the inversion process are listed in Algorithm 1.

Algorithm 1 Inversion process

1: Define the frequency range and the number of frequency points N in the target band gap
2: Define the geometry of the unit cell (e.g. period, number of distinct material elements, etc.)
3: Set the initial search length
4: Set initial guess for the material properties ρ_0 and μ_0
5: Set $N_D = 0$
6: Initialize the iteration counter $l \leftarrow 0$
7: **for** $N_D < N$ **do**
8: Solve the state eigenvalue problem ▷ Eq. (18)
9: Compute N_D ▷ Eq. (23)
10: Solve the adjoint eigenvalue problem ▷ Eq. (19)
11: Compute the gradient of L ▷ Eq. (20)
12: Obtain the search direction (e.g., conjugate gradient method)
13: Update the material properties ρ_{l+1} and μ_{l+1} using backtracking algorithm; stop if sufficient-decrease condition is violated
14: Set $l \leftarrow l + 1$.
15: **end for**

3.6. Extensions for topology design

Thus far, in the outlined inversion methodology, it is only the material parameters ρ and μ that have been considered as unknown design variables, whereas the topology of the unit cell has been considered fixed (the material thicknesses are set *a priori*). However, the same framework can be used to accommodate unknown thicknesses (or, more generally, unknown topology), with the addition of an equality constraint to the Lagrangian (the sum of the thicknesses must equal the size of the unit cell), and suitable modifications to the control problem. Specifically, of the three optimality conditions discussed in Section 3.3, the state and adjoint eigenvalue problems would remain the same, but the gradients of L (the control problem) would have to be complemented by the derivatives of L with respect to the unknown thicknesses. Thus, it would be possible to simultaneously invert for both the topology and the properties, using the same discriminant-based objective functional.

4. Generalization to higher spatial dimensions

We claim that the discriminant-based objective functional (14) can also be used to drive the inverse design problem for scalar waves in higher dimensions, since the negativity of the discriminant is still a unique indicator of a band gap owing to the fact that the associated sesquilinear forms, $a_0(v, u)$, $a_1(v, u)$, and $a_2(v, u)$, remain Hermitian. Higher spatial dimensions introduce additional complexities associated with the presence of multiple directions (in wavenumber space), and multiple modes. Yet, as it will be discussed, the inversion framework presented in Section 3 is capable of accommodating multiple modes and multiple user-defined directions, including omni-directional band gap targets.

To fix ideas, consider the n-dimensional ($n = 2, 3$) scalar Helmholtz equation:

$$\text{div}\,[\mu(\boldsymbol{x})\text{grad}\,U(\boldsymbol{x})] + \omega^2\rho(\boldsymbol{x})U(\boldsymbol{x}) = 0,\ \ \forall \boldsymbol{x} \in \mathbb{R}^n, \tag{26}$$

with the periodicity relations $\mu\left(\boldsymbol{x} + \sum_{i=1}^{n} m_i\mathbf{p}_i\right) = \mu(\boldsymbol{x})$ and $\rho\left(\boldsymbol{x} + \sum_{i=1}^{n} m_i\mathbf{p}_i\right) = \rho(\boldsymbol{x}), \forall m_i \in \mathbb{Z}$; $\mathbf{p}_i \in \mathbb{R}$ are primitive lattice vectors, which define the metamaterial topology when given a unit cell. Then, the Bloch theorem suggests

$$U(\boldsymbol{x}) = u(\boldsymbol{x})e^{\mathrm{i}\mathbf{k}\cdot\boldsymbol{x}}, \tag{27}$$

where $u\left(\boldsymbol{x} + \sum_{i=1}^{n} m_i\mathbf{p}_i\right) = u(\boldsymbol{x})$, and $\mathbf{k}$ denotes wavevector.

4.1. Eigenvalue problem and band structure

Following lines similar to those described in Section 2.2, and while setting $\mathbf{k} = k\mathbf{d} + \mathbf{d}_0$, we obtain the weak form of the quadratic eigenvalue problem corresponding now to the n-dimensional equation (26):
Given ω, $\mathbf{d}$, and $\mathbf{d}_0$, find $k \in \mathbb{C}$ and $u \in \mathcal{W} \setminus \{0\}$ such that

$$0 = a_0(v,u) + ka_1(v,u) + k^2 a_2(v,u) \equiv P(k)(v,u) \quad \forall v \in \mathcal{W}, \tag{28}$$

where

$$\mathcal{W} = \left\{ u \in H^1(\Omega) \,\middle|\, u(\boldsymbol{x}) = u\left(\boldsymbol{x} + \sum_{i=1}^{n} m_i \mathbf{p}_i\right) \ \forall \boldsymbol{x} \in \partial\Omega \right\}, \tag{29a}$$

$$a_0(v,u) = \int_\Omega \left[\operatorname{grad}\overline{v} \cdot \operatorname{grad} u - \overline{v}\omega^2 \rho\, u\right] d\Omega + \mathrm{i}\int_\Omega \left[\operatorname{grad}\overline{v} \cdot \mu\mathbf{d}_0 u - \mathbf{d}_0\overline{v} \cdot \mu \operatorname{grad} u\right] d\Omega + \int_\Omega \mathbf{d}_0\overline{v} \cdot \mu\mathbf{d}_0 u d\Omega, \tag{29b}$$

$$a_1(v,u) = \mathrm{i}\int_\Omega \left[\operatorname{grad}\overline{v} \cdot \mu\mathbf{d}u - \mathbf{d}\overline{v} \cdot \mu \operatorname{grad} u\right] d\Omega + \int_\Omega \left[\mathbf{d}\overline{v} \cdot \mu\mathbf{d}_0 u + \mathbf{d}_0\overline{v} \cdot \mu\mathbf{d}u\right] d\Omega, \text{ and} \tag{29c}$$

$$a_2(v,u) = \int_\Omega \mathbf{d}\overline{v} \cdot \mu\mathbf{d}u d\Omega. \tag{29d}$$

In the above, Ω is the domain of the unit cell and $\partial\Omega$ is its boundary. Then, the complex band structure can be obtained by solving (28) for different choices of direction $\mathbf{d}$ and offset $\mathbf{d}_0$ (the offset $\mathbf{d}_0$ is required for the high-symmetry line that is not connected to the center of the Brillouin zone Γ, otherwise $\mathbf{d}_0 = \mathbf{0}$). For example, for a square unit cell with a typical triangular irreducible Brillouin zone, we use $\mathbf{d} = (1, 0)$ and $\mathbf{d}_0 = \mathbf{0}$ for Γ-X; $\mathbf{d} = (1/\sqrt{2}, 1/\sqrt{2})$ and $\mathbf{d}_0 = \mathbf{0}$ for Γ-M; and $\mathbf{d} = (0, 1)$ and $\mathbf{d}_0 = (1, 0)$ for X-M.

Similarly to the one-dimensional case, we are interested in comparing the complex band structure to the one obtained by considering the sign of the problem's discriminant. The discriminant, using (28), is again expressed in terms of the sesquilinear forms, as:

$$\mathcal{D} = a_1(u,u)a_1(u,u) - 4a_0(u,u)a_2(u,u). \tag{30}$$

To highlight the equivalency between the complex band structure and the discriminant sign, we focus on a prototype square unit cell, as shown in Fig. 4(b). The unit cell consists of a square inclusion of dimensions (0.5×0.5) embedded concentrically within a square of unit sides. The properties of the inclusion are $\rho_1 = 1.9$, $\mu_1 = 1.7$, whereas the background medium has $\rho_2 = 0.5$ and $\mu_2 = 0.6$. The figure's gray shading is driven by the wave speeds of the two media ($c_1 = 0.95$ and $c_2 = 1.1$). Figs. 4(a) and 4(c) depict the real and imaginary part, respectively, of the complex band structure that was obtained by solving the quadratic eigenvalue problem (28), plotted along the high-symmetry lines of the irreducible Brillouin zone (see insert in Fig. 4(a)).

The shaded zones in both Figs. 4(a) and 4(c) correspond to band gaps, and are characterized by a nonzero imaginary part ($\Im m\{\hat{k}\} \neq 0$). We note that there are multiple modes depicted in the figures. More interestingly, Fig. 4(d) depicts the discriminant for each of the modes shown in the complex band structure and for the same range of frequencies. We note that the regions where all modal discriminants are negative coincide with the band gaps shown in the complex band structure.

4.2. Lagrangian In higher dimensions

To define the Lagrangian in higher dimensions, we follow the concepts outlined in the one-dimensional formulation of Section 3.2, while accounting for multiple directions and multiple modes. We denote the number of directions by n_d and the number of modes by n_m. Thus, we replace the one-dimensional definitions (24) and (25) for the objective functional and the constraint, respectively, using conditional summations, to yield:

$$D[\rho,\mu,u] = \sum_i^N \sum_j^{n_d} \left[\sum_{s|\mathcal{D}_s^{(i,j)}>0}^{n_m} \mathcal{D}_s^{(i,j)} \right] \quad \text{and} \tag{31}$$

$$E[\rho,\mu,u,k,v,\xi] = \sum_i^N \sum_j^{n_d} \left[\sum_{s|\mathcal{D}_s^{(i,j)}>0}^{n_m} \Re e\left\{ P\left(k_s^{(i,j)}\right)\left(v_s^{(i,j)}, u_s^{(i,j)}\right)\right\} \right] + \sum_i^N \sum_j^{n_d} \left[\sum_{s|\mathcal{D}_s^{(i,j)}>0}^{n_m} \frac{\xi_s^{(i,j)}}{2}\left[a_2\left(u_s^{(i,j)}, u_s^{(i,j)}\right) - 1\right] \right]. \tag{32}$$

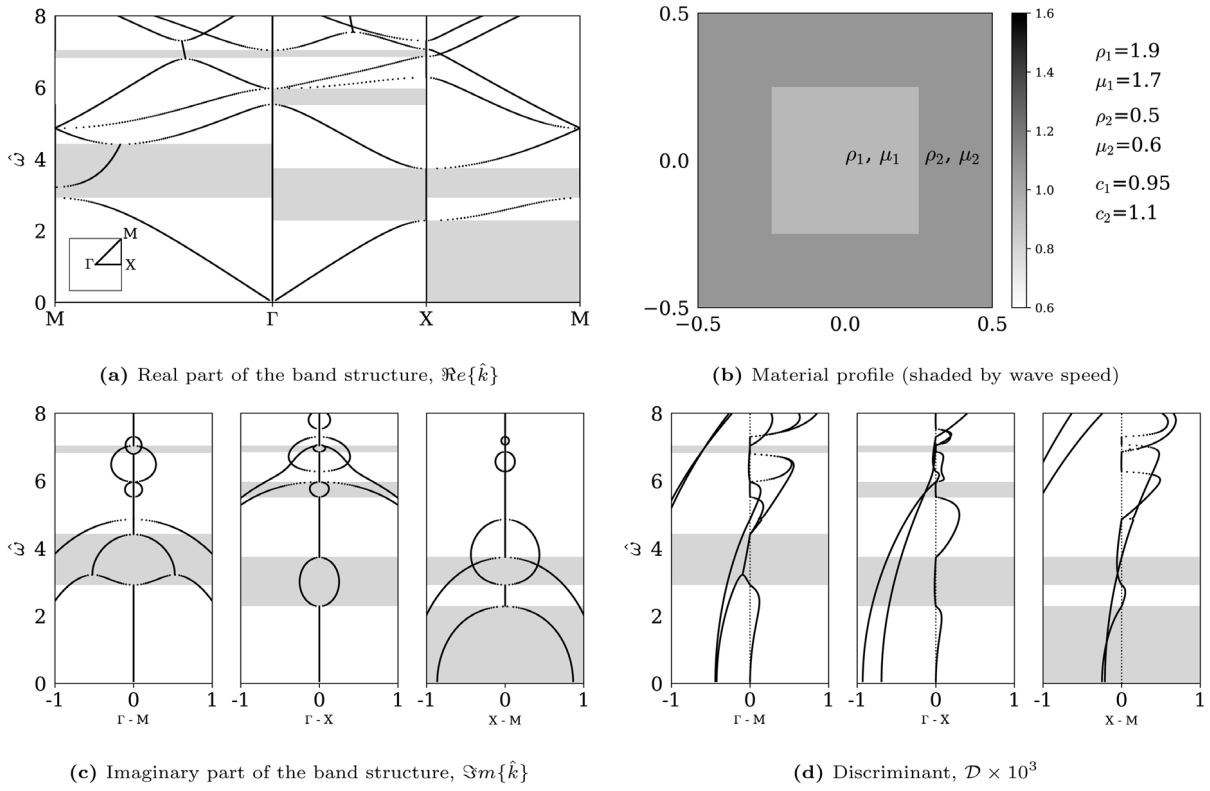

(a) Real part of the band structure, $\Re e\{\hat{k}\}$

(b) Material profile (shaded by wave speed)

(c) Imaginary part of the band structure, $\Im m\{\hat{k}\}$

(d) Discriminant, $\mathcal{D} \times 10^3$

Fig. 4. (a), (c): Real and imaginary parts of a typical band structure of a two-dimensional scalar wave problem; (b) unit cell topology and material properties; (d) discriminant of the associated quadratic eigenvalue problem. Multiple modes are present in each direction; band gaps are observed where all modal discriminants are negative (gaps highlighted with gray shading).

In the above, index i is used to denote different temporal frequencies $\omega^{(i)}$ ($i = 1, \ldots, N$), index j is used to denote different directions $\mathbf{d}^{(j)}$ ($j = 1, \ldots, n_d$), and s is used to denote the sth modal quantities (k_s, u_s of the state pair, and ξ_s, v_s of the adjoint pair), with $s = 1, \ldots, n_m$. The higher-dimensional Lagrangian is defined again as $L = D + E$.

The conditional summation in (31) implies, by construction, a lower bound for the objective functional D, and allows for a simple termination criterion, as discussed in Section 3.4. We note that if a uni-directional band gap is aimed for, then $n_d = 1$, whereas for an omni-directional band gap, $n_d > 1$. In general, the minimum number for n_d depends on the topology and the sought type of band gap (uni-, multi-, or omni-directional). In our experience, driving the inversion with directions from the origin to the high-symmetry points of the Brillouin zone proved sufficient for an omni-directional band gap, without requiring multiple directions spanning the entire Brillouin zone. For example, in the case of the square unit cell, $\mathbf{d}^{(1)} = (1, 0)$ (from Γ to X) and $\mathbf{d}^{(2)} = (1/\sqrt{2}, 1/\sqrt{2})$ (from Γ to M), are sufficient for an omni-directional band gap.

4.3. Optimality conditions

The first-order optimality conditions are obtained similarly to the one-dimensional case, by enforcing the vanishing of the Lagrangian's first derivatives. There results:

1. **State eigenvalue problem**
   Given ρ and μ, find $k_s^{(i,j)} \in \mathbb{C}$ and $u_s^{(i,j)} \in \mathcal{W} \setminus \{0\}$ such that

$$0 = P\left(k_s^{(i,j)}\right)\left(\tilde{v}_s^{(i,j)}, u_s^{(i,j)}\right) \quad \forall \tilde{v}_s^{(i,j)} \in \mathcal{W} \tag{33a}$$

$$0 = \frac{\tilde{\xi}_s^{(i,j)}}{2}\left[a_2\left(u_s^{(i,j)}, u_s^{(i,j)}\right) - 1\right] \quad \forall \tilde{\xi}_s^{(i,j)} \in \mathbb{R}. \tag{33b}$$

2. **Adjoint eigenvalue problem**
   Given ρ, μ, $k_s^{(i,j)}$, and $u_s^{(i,j)}$, find $\xi_s^{(i,j)} \in \mathbb{R}$ and $v_s^{(i,j)} \in \mathcal{W}$ such that

$$0 = P\left(k_s^{(i,j)}\right)\left(v_s^{(i,j)}, \tilde{u}_s^{(i,j)}\right) + \xi_s^{(i,j)} a_2\left(u_s^{(i,j)}, \tilde{u}_s^{(i,j)}\right) + 4a_1\left(u_s^{(i,j)}, u_s^{(i,j)}\right) a_1\left(u_s^{(i,j)}, \tilde{u}_s^{(i,j)}\right)$$

$$- \; 8a_2\left(u_s^{(i,j)}, u_s^{(i,j)}\right) a_0\left(u_s^{(i,j)}, \tilde{u}_s^{(i,j)}\right) - 8a_0\left(u_s^{(i,j)}, u_s^{(i,j)}\right) a_2\left(u_s^{(i,j)}, \tilde{u}_s^{(i,j)}\right) \;\; \forall \tilde{u}_s^{(i,j)} \in \mathcal{W} \tag{34a}$$

$$0 = \tilde{k}_s^{(i,j)} a_1\left(v_s^{(i,j)}, u_s^{(i,j)}\right) + 2\tilde{k}_s^{(i,j)} k_s^{(i,j)} a_2\left(v_s^{(i,j)}, u_s^{(i,j)}\right) \;\; \forall \tilde{k}_s^{(i,j)} \in \mathbb{C}. \tag{34b}$$

3. **Gradient of L**
Given ρ, μ, $k_s^{(i,j)}$, $u_s^{(i,j)}$, $\xi_s^{(i,j)}$ and $v_s^{(i,j)}$, find $g_\rho \in \mathcal{T}$ and $g_\mu \in \mathcal{T}$ such that

$$\begin{aligned}
\int_\Omega \tilde{\rho}\, g_\rho d\Omega = &\sum_i^N \sum_j^{n_d} \sum_{s|\mathcal{D}_s^{(i,j)}>0}^{n_m} \Re e\left\{4a_2\left(u_s^{(i,j)}, u_s^{(i,j)}\right) \int_\Omega \overline{u}_s^{(i,j)} \omega^2 \tilde{\rho}\, u_s^{(i,j)} d\Omega\right\} \\
&- \sum_i^N \sum_j^{n_d} \sum_{s|\mathcal{D}_s^{(i,j)}>0}^{n_m} \Re e\left\{\int_\Omega \overline{v}_s^{(i,j)} \omega^2 \tilde{\rho}\, u_s^{(i,j)} d\Omega\right\} \;\; \forall \tilde{\rho} \in \mathcal{T}
\end{aligned} \tag{35a}$$

$$\begin{aligned}
\int_\Omega \tilde{\mu}\, g_\mu d\Omega = &\sum_i^N \sum_j^{n_d} \sum_{s|\mathcal{D}_s^{(i,j)}>0}^{n_m} \Re e\left\{2a_1\left(u_s^{(i,j)}, u_s^{(i,j)}\right) \int_\Omega \mathrm{i}\left(\operatorname{grad} \overline{u}_s^{(i,j)} \cdot \tilde{\mu}\, \mathbf{d}^{(j)} u_s^{(i,j)}\right.\right. \\
&\left.\left. - \mathbf{d}^{(j)} \overline{u}_s^{(i,j)} \cdot \tilde{\mu} \operatorname{grad} u_s^{(i,j)}\right) d\Omega\right\} \\
&- \sum_i^N \sum_j^{n_d} \sum_{s|\mathcal{D}_s^{(i,j)}>0}^{n_m} \Re e\left\{4a_2\left(u_s^{(i,j)}, u_s^{(i,j)}\right) \int_\Omega \operatorname{grad} \overline{u}_s^{(i,j)} \cdot \tilde{\mu} \operatorname{grad} u_s^{(i,j)} d\Omega\right\} \\
&- \sum_i^N \sum_j^{n_d} \sum_{s|\mathcal{D}_s^{(i,j)}>0}^{n_m} \Re e\left\{4a_0\left(u_s^{(i,j)}, u_s^{(i,j)}\right) \int_\Omega \overline{u}_s^{(i,j)} \tilde{\mu}\, u_s^{(i,j)} d\Omega\right\} \\
&+ \sum_i^N \sum_j^{n_d} \sum_{s|\mathcal{D}_s^{(i,j)}>0}^{n_m} \Re e\left\{k_s^{(i,j)} \int_\Omega \mathrm{i}\left(\operatorname{grad} \overline{v}_s^{(i,j)} \cdot \tilde{\mu}\, \mathbf{d}^{(j)} u_s^{(i,j)}\right.\right. \\
&\left.\left. - \mathbf{d}^{(j)} \overline{v}_s^{(i,j)} \cdot \tilde{\mu} \operatorname{grad} u_s^{(i,j)}\right) d\Omega\right\} \\
&+ \sum_i^N \sum_j^{n_d} \sum_{s|\mathcal{D}_s^{(i,j)}>0}^{n_m} \Re e\left\{\int_\Omega \operatorname{grad} \overline{v}_s^{(i,j)} \cdot \tilde{\mu} \operatorname{grad} u_s^{(i,j)} d\Omega\right\} \\
&+ \sum_i^N \sum_j^{n_d} \sum_{s|\mathcal{D}_s^{(i,j)}>0}^{n_m} \Re e\left\{\left(k_s^{(i,j)}\right)^2 \int_\Omega \overline{v}_s^{(i,j)} \tilde{\mu}\, u_s^{(i,j)} d\Omega\right\} \\
&+ \sum_i^N \sum_j^{n_d} \sum_{s|\mathcal{D}_s^{(i,j)}>0}^{n_m} \Re e\left\{\frac{\xi_s^{(i,j)}}{2} \int_\Omega \overline{u}_s^{(i,j)} \tilde{\mu}\, u_s^{(i,j)} d\Omega\right\} \;\; \forall \tilde{\mu} \in \mathcal{T},
\end{aligned} \tag{35b}$$

where

$$\mathcal{T} = \left\{ u \in H^0(\Omega) \,\middle|\, u(\boldsymbol{x}) = u\left(\boldsymbol{x} + \sum_{i=1}^n m_i \mathbf{p}_i\right) \;\; \forall \boldsymbol{x} \in \partial\Omega \right\}. \tag{36}$$

We note that the 1D inversion process described in Section 3.5 remains, largely, the same.

5. Numerical examples

In this section, we demonstrate the performance of the band-gap-driven material inversion with numerical examples in one and two dimensions. We discuss first the one-dimensional cases.

We perform inversions with different target band-gap ranges and different unit-cell material arrangements. All inversions are performed in the frequency-domain; a time-domain simulation with the (multi-cell) metamaterial that resulted from the inversion methodology is also included to attest to the effect the metamaterial has in arresting the propagation of the targeted frequency band.

The objective functional (13) is capable of accommodating various material arrangements. Herein, for most of the numerical examples, we fix the topology, i.e., we constrain the number of different materials and their respective extent within the unit cell, using piecewise constant approximations for the density ρ and the modulus μ. We note that a continuously-varying or functionally-graded material can also be accommodated, as it will be shown, by simply increasing the number of allowed materials within the unit cell.

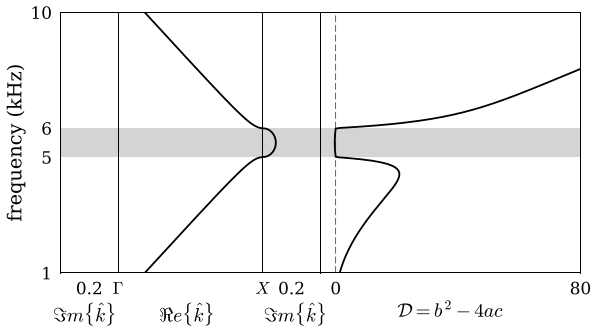

(a) Band structure (left) and discriminant (right)

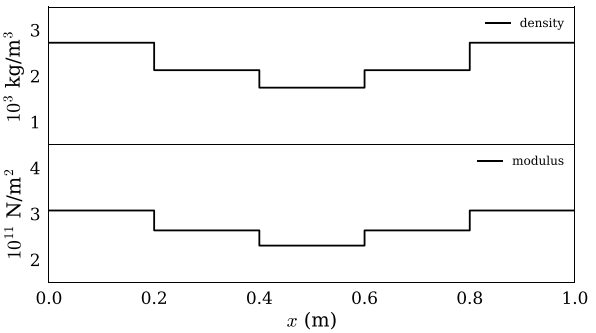

(b) Unit-cell density and modulus distribution

Fig. 5. Inversion for 5 material elements with a target band gap of 5–6 kHz.

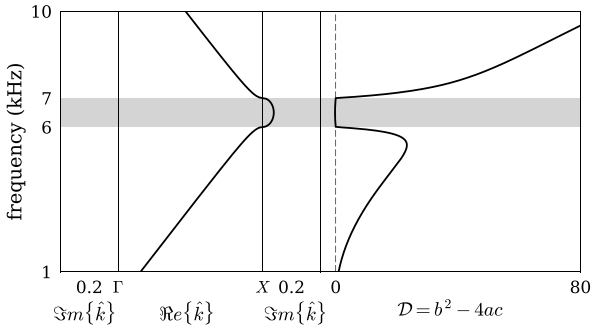

(a) Band structure (left) and discriminant (right)

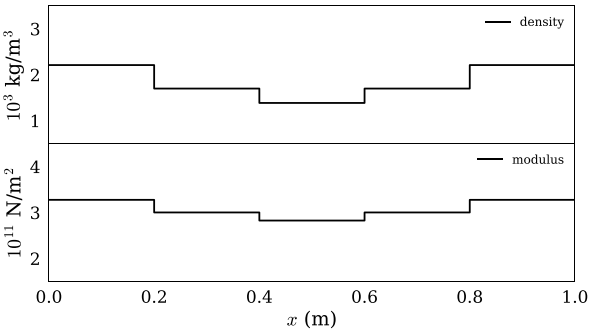

(b) Unit-cell density and modulus distribution

Fig. 6. Inversion for 5 material elements with a target band gap of 6–7 kHz.

We choose the same initial guesses for ρ and μ for all one-dimensional examples, thus setting $\rho = 3000$ kg/m^3 and $\mu = 2.0 \times 10^{11}$ N/m^2. The length of the unit cell is set to 1 m. We use standard quadratic elements to approximate the state and adjoint eigenfunctions. Small perturbations (of unit magnitude) are added to the material properties of all elements of the mesh except for the two out-most elements, in order not to start the inversion with a perfectly homogeneous initial guess (if the initial guess is homogeneous, the inversion will yield a constant gradient due to the periodicity). We use PETSc [22]. and SLEPc [23,24] to implement the inversion.

5.1. Band-gap targets with different central frequencies

We invert first for a unit cell comprising 5 materials, and for band gaps exhibiting the same gap width (1000 Hz), but different central frequencies (5500 Hz, 6500 Hz, and 7500 Hz, respectively). Specifically, Figs. 5, 6, and 7 depict the results for band gaps of 5000–6000 Hz, 6000–7000 Hz, and 7000–8000 Hz, respectively. In all three figures, the left column shows both the Brillouin zone and the discriminant as a function of frequency, while the band-gap region is shown as shaded. The right column shows the inverted material profile (density and modulus) responsible for the resulting band gap. It can be seen that in all cases the targeted band-gap regions have been sharply recovered.

5.2. Band-gap targets with different frequency width

We perform inversions with different target frequency widths using again 5 material elements. Figs. 8 and 9 show the results for band gaps in the 5000–7000 Hz, and 5000–9000 Hz range, respectively. Both the narrow (2 kHz) and the wider (4 kHz) band gaps are well delineated, as shown with the shaded regions. Notice that in the first case (Fig. 8), the first gap that appears in the band structure is the target band gap; however, in the second case (Fig. 9), the inversion led to a unit cell that exhibits a first gap at lower frequencies (around 3 kHz) than the target gap, in addition to the target band gap (5–9 kHz).

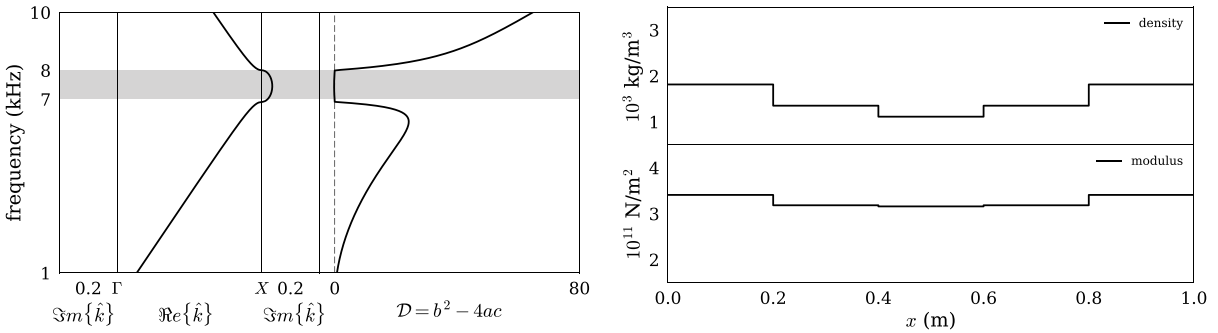

(a) Band structure (left) and discriminant (right)

(b) Unit-cell density and modulus distribution

Fig. 7. Inversion for 5 material elements with a target band gap of 7–8 kHz.

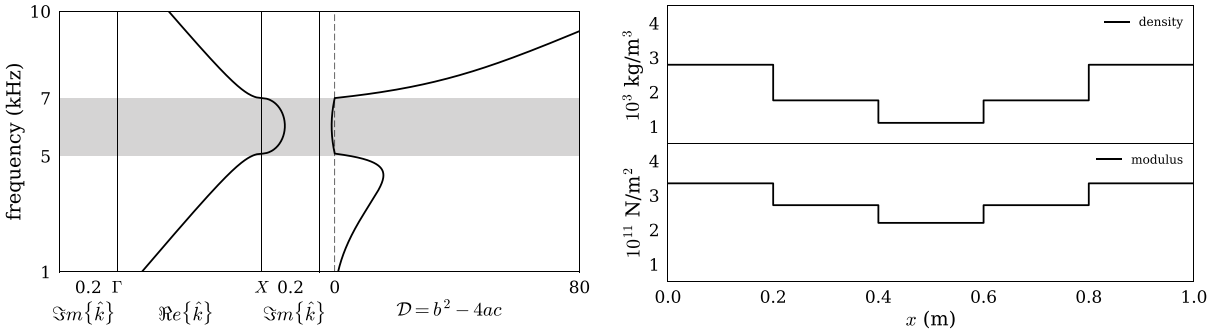

(a) Band structure (left) and discriminant (right)

(b) Unit-cell density and modulus distribution

Fig. 8. Inversion for 5 material elements with a target band gap of 5–7 kHz .

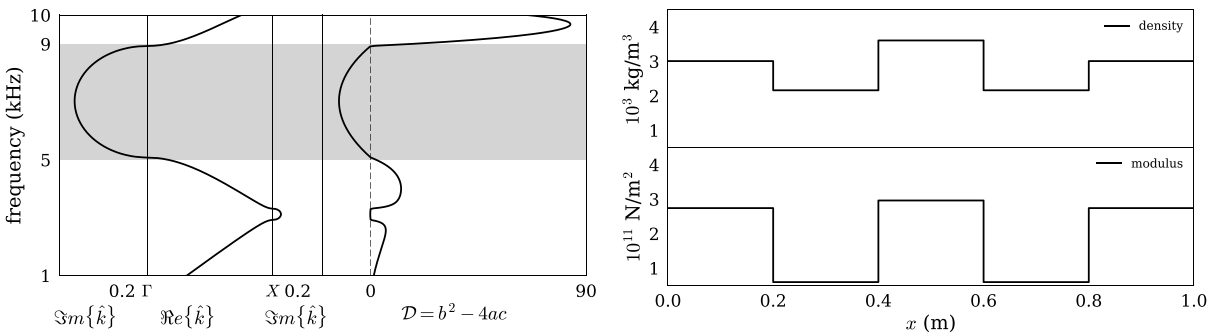

(a) Band structure (left) and discriminant (right)

(b) Unit-cell density and modulus distribution

Fig. 9. Inversion for 5 material elements with a target band gap of 5–9 kHz.

5.3. Band-gap targets with different number of unit-cell material elements

Next, we relax the 5-material constraint for the unit cell to allow for 40 different piecewise-constant materials of equal thickness, thus approximating a materially continuously-varying unit cell. The desired band gap is set to 5000–6000 Hz. Fig. 10 depicts the resulting density and modulus unit-cell distributions, alongside with the band-gap structure. Moreover, Fig. 11 shows the resulting material distribution when the material constraint for the unit cell has been reinstated and set to 3. We note that the band-gap structures are identical between the two cases: this is evidence of multiplicity, i.e., different unit-cell material arrangements are capable of exhibiting the same band-gap. In practice, manufacturing constraints on the number and/or the type of materials could drive the inversion for a fixed topology.

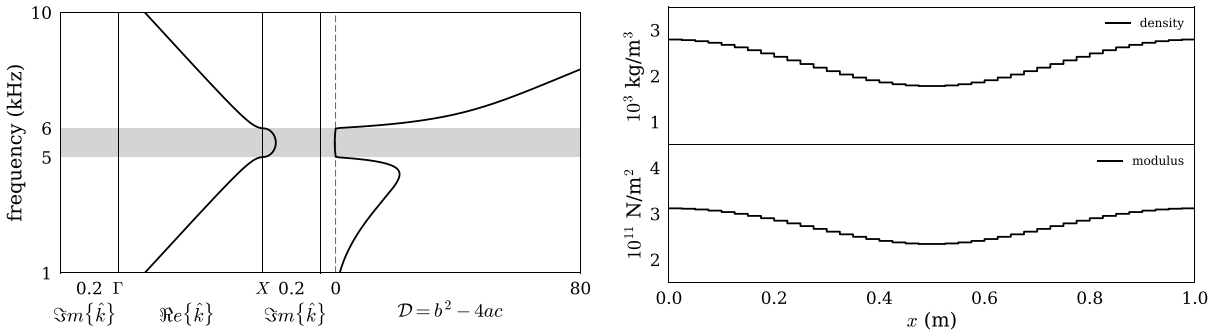

(a) Band structure (left) and discriminant (right)

(b) Unit-cell density and modulus distribution

Fig. 10. Inversion for 40 material elements with a target band gap of 5–6 kHz.

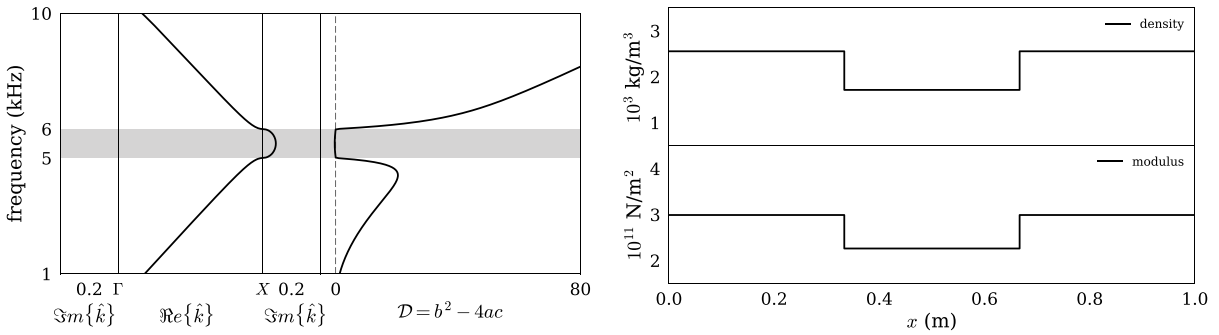

(a) Band structure (left) and discriminant (right)

(b) Unit-cell density and modulus distribution

Fig. 11. Inversion for 3 material elements with a target band gap of 5–6 kHz.

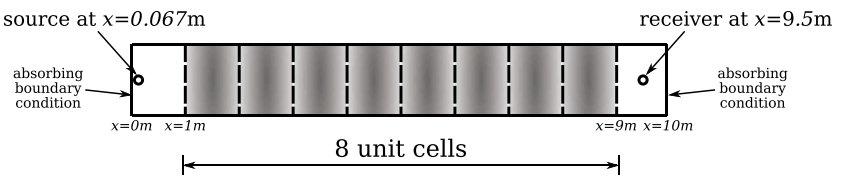

Fig. 12. Metamaterial time-domain simulation schematic.

5.4. Metamaterial time-domain simulations

Next, we use the inverted 5-material unit cell design depicted in Fig. 8(b) to construct a metamaterial by stacking 8 unit cells (8 m-long) together, within a 10 m-long domain (Fig. 12). We subject the metamaterial block to a dichromatic sinusoidal load given by:

$$f(t) = \sin(2\pi f_1 t) + \sin(2\pi f_2 t), \tag{37}$$

where $f_1 = 6000$ Hz and $f_2 = 2000$ Hz. Near the origin and to the left of the applied source (source at $x = 0.067$m) and at $x = 10$m we apply absorbing boundary conditions (Fig. 12). The selected unit cell exhibits, by virtue of the inverse design, a band gap between 5000–7000 Hz. Thus, the propagation of f_1 should be arrested, and the resulting signal should be monochromatic at the f_2 frequency. Fig. 13 depicts the time-domain results. The first-row figures (Figs. 13(a) and 13(b)) depict the response of a homogeneous medium. By comparing the signal at the entry point ($x = 0$m) with the signal at the domain end ($x = 10$m) in the waterfall plot, it can be seen that the dichromatic signal's frequency content remains intact during the propagation. By contrast, the waterfall plot in Fig. 13(c), which corresponds to the metamaterial, shows that the entering dichromatic signal was reduced to a monochromatic signal at exit, with only the f_2 frequency component surviving, as intended. To illustrate the effect with broader-band driving signals, we next subject the same metamaterial structure to

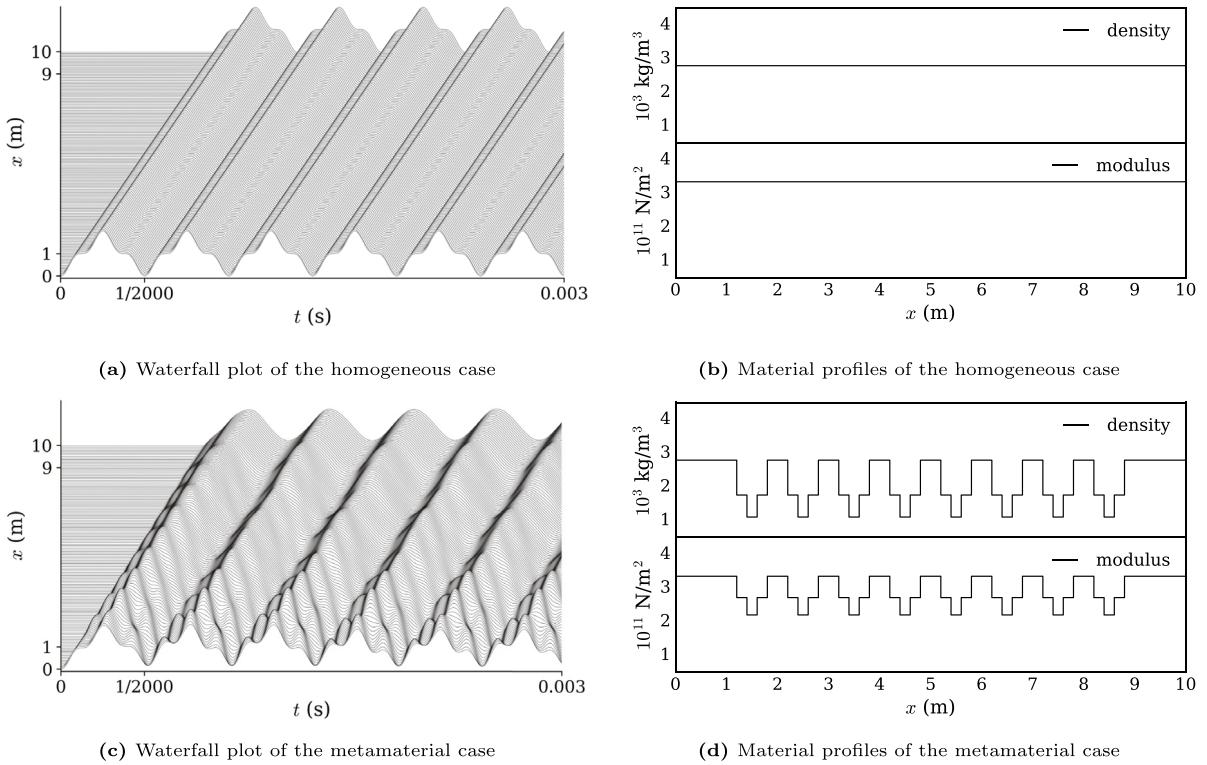

(a) Waterfall plot of the homogeneous case

(b) Material profiles of the homogeneous case

(c) Waterfall plot of the metamaterial case

(d) Material profiles of the metamaterial case

Fig. 13. Time-domain simulation of a metamaterial block subjected to a dichromatic load: (a) dichromatic signal with $f_1 = 2000$ Hz and $f_2 = 6000$ Hz propagates within the homogeneous medium without frequency component loss; (c) dichromatic signal is reduced to a monochromatic signal when propagating through the metamaterial block ($f_2 = 6000$ Hz is arrested).

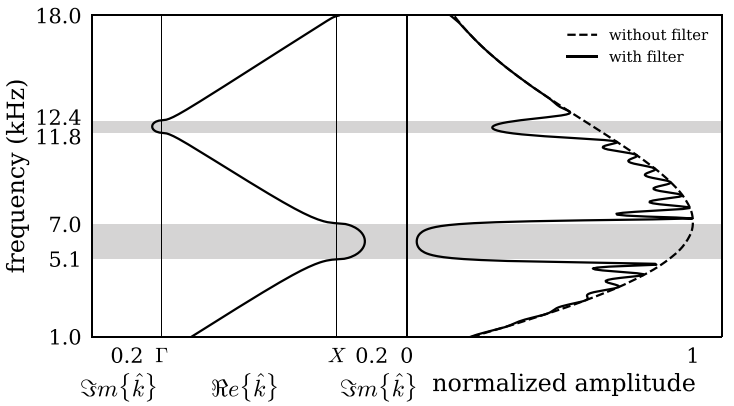

Fig. 14. DFT response of a homogeneous material and metamaterial subjected to a Ricker pulse: waves are attenuated at the band-gap regions (highlighted with shades).

a Ricker pulse with a central frequency at 10 kHz. The Ricker pulse is defined as:

$$f(t) = \frac{(0.25u^2 - 0.5)e^{-0.25u^2} - 13e^{-13.5}}{0.5 + 13e^{-13.5}}, \ 0 \le t \le \frac{6\sqrt{6}}{\omega_r}, \tag{38}$$

where $u = \omega_r t - 3\sqrt{6}$ and $\omega_r = 2\pi \cdot 10000$ is the central circular frequency. The response is again recorded at $x = 10$m and its discrete Fourier Transform is shown in Fig. 14 together with the band structure. The dashed line represents the DFT of the homogeneous material response, whereas the solid line represents the DFT of the metamaterial response. We note that the band gap between 5–7 kHz worked well by forcing the response to near silence. Notice that the metamaterial exhibits a second band gap between 11.8–12.4 kHz, which also had an amplitude-reducing effect on the response.

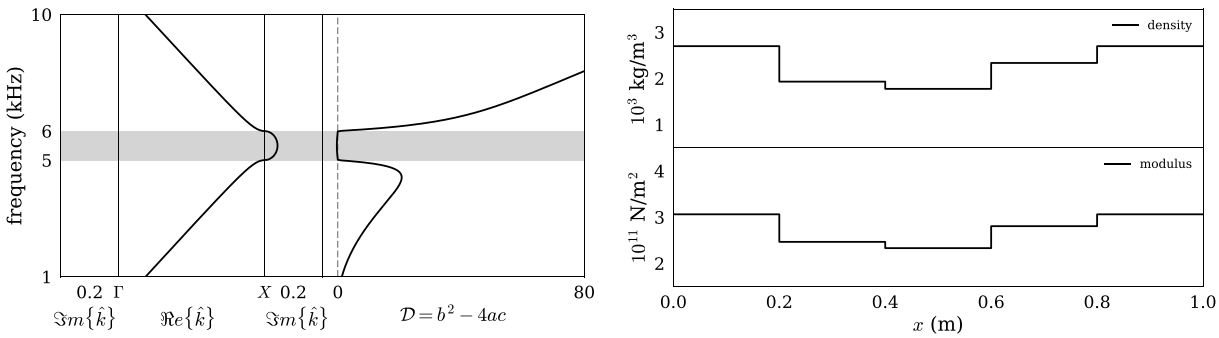

(a) Band structure (left) and discriminant (right)

(b) Unit-cell density and modulus distribution

Fig. 15. Inversion for 5 material elements with a target frequency range of 5–6 kHz: asymmetric material properties are obtained by asymmetric initial guesses.

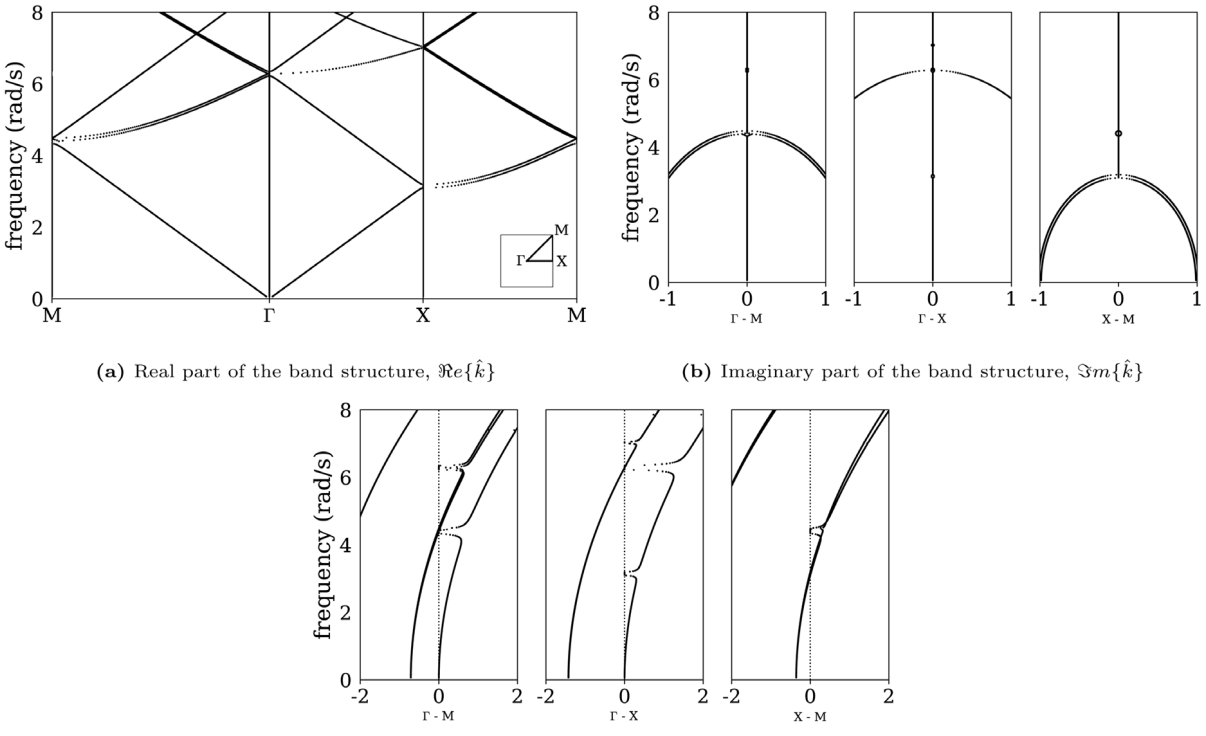

(a) Real part of the band structure, $\Re e\{\hat{k}\}$

(b) Imaginary part of the band structure, $\Im m\{\hat{k}\}$

(c) Discriminant, $\mathcal{D} \times 10^3$

Fig. 16. Complex band structure and discriminant of the initial guess.

Asymmetric material profiles. The preceding examples have all resulted in symmetric material profiles. This is due to the fact that the initial guesses were symmetric. Using asymmetric distributions as initial guesses, one can obtain asymmetric material profiles through inversion. To illustrate, we start with an initial guess with the same amount of perturbation on the properties as the one we used for all the preceding examples. However, in this case we perturb only the properties of the second element to force an asymmetric initial guess. The results are depicted in Fig. 15). The target band-gap region is identical to the one we obtained previously (Fig. 5), yet the recovered unit-cell is asymmetric.

5.5. Omni-directional band gap design in 2D

We discuss the application of the inversion methodology to two dimensions. Our reference unit cell is a square with sides p, with a concentrically embedded square inclusion with sides equal to $0.5p$. Under this fixed topology, we seek to invert

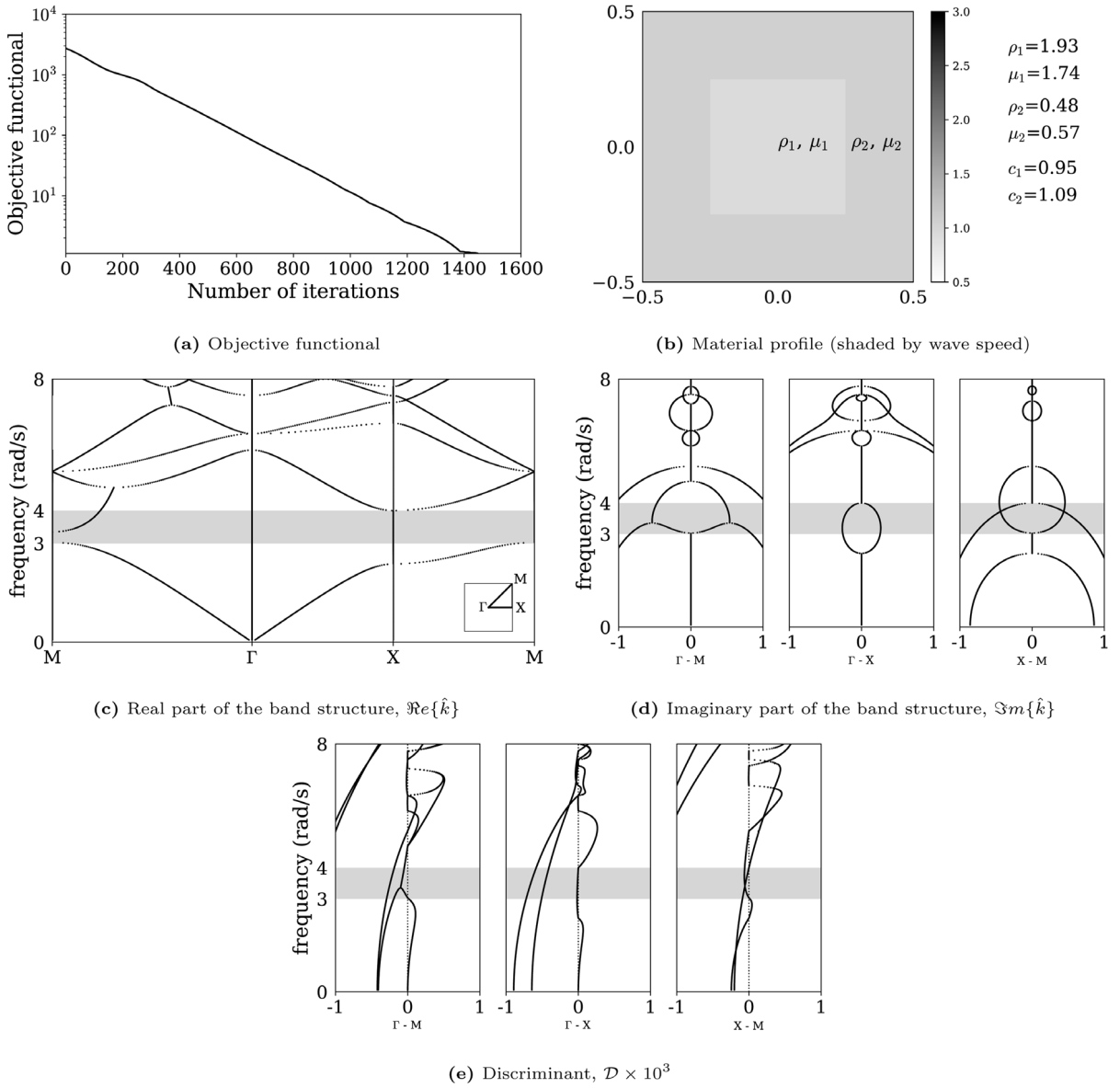

(a) Objective functional

(b) Material profile (shaded by wave speed)

(c) Real part of the band structure, $\Re e\{\hat{k}\}$

(d) Imaginary part of the band structure, $\Im m\{\hat{k}\}$

(e) Discriminant, $\mathcal{D} \times 10^3$

Fig. 17. Inversion for 2 materials elements for an omni-directional band gap at 3–4 rad/s; band gap shown shaded.

for the material properties of both the inclusion (ρ_1 and μ_1) and of the background square host (ρ_2 and μ_2). The primitive lattice vectors are $\mathbf{p}_1 = (1, 0)$ and $\mathbf{p}_2 = (0, 1)$, where $\|\mathbf{p}_1\| = \|\mathbf{p}_2\| = 1 \equiv p$. We are interested in an omni-directional band gap, and to this end, we use two directions ($n_d = 2$), $\mathbf{d}^{(1)} = (1, 0)$ (Γ to X), and $\mathbf{d}^{(2)} = (1/\sqrt{2}, 1/\sqrt{2})$ (Γ to M). We set the number of modes to $n_m = 4$, and the number of frequencies in the target band gap to $N = 30$. We discuss three examples with different target band gaps: 3–4, 4–5, and 4–6 rad/s.

We start with the initial material profile of $\rho_1 = 1.1$, $\mu_1 = 1.1$, $\rho_2 = 1.0$, and $\mu_2 = 1.0$ for all three examples. The band structure of the initial guess is shown in Fig. 16: it is very similar to that of a homogeneous medium, exhibiting, however, narrow directional band gaps and degeneracy breakings.

Figs. 17, 18, and 19 show the results of the inverse designs for the different target band gaps, 3–4, 4–5, and 4–6 rad/s, respectively. In each figure, subplots (a) show the trajectory of the objective functional as the number of iterations increases (semi-log plot): there is, roughly, a four-order reduction from the initial guess. Subplots (b) show the converged material profile, i.e., the inverted-for material parameters ρ_1, μ_1, ρ_2, and μ_2 (the shading is driven by the wave speeds). Subplots (c) show the real part, while subplots (d) show the imaginary part of the band structure of the designed unit cell. Subplots (e) show the associated discriminant. As it can be seen, in all cases, the targeted omni-directional band gaps (shown in subplots (c), (d), and (e) with shaded strips) have been realized.

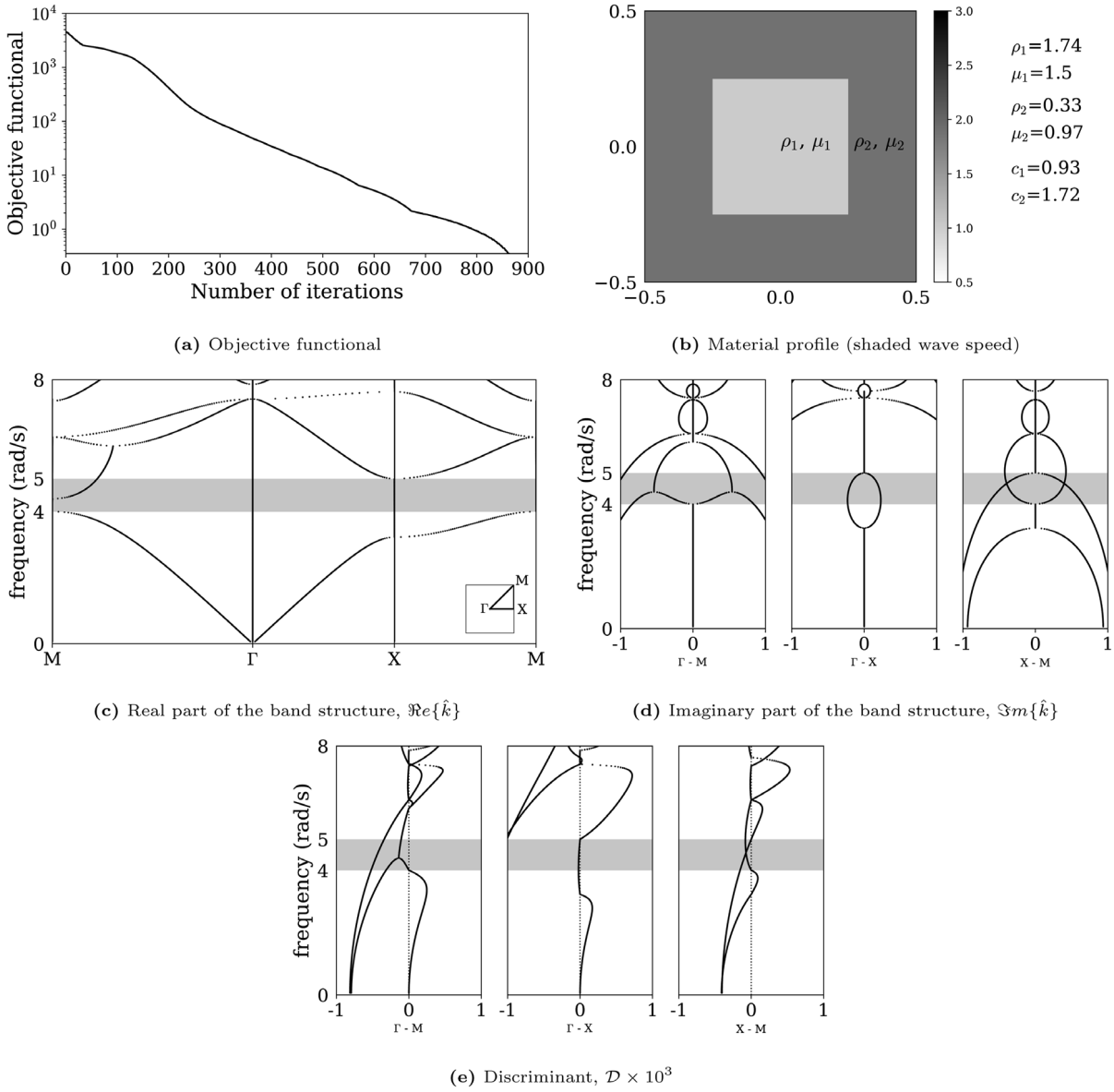

(a) Objective functional

(b) Material profile (shaded wave speed)

(c) Real part of the band structure, $\Re e\{\hat{k}\}$

(d) Imaginary part of the band structure, $\Im m\{\hat{k}\}$

(e) Discriminant, $\mathcal{D} \times 10^3$

Fig. 18. Inversion for 2 materials elements for an omni-directional band gap at 4–5 rad/s; band gap shown shaded.

We note that, in all cases, an, unduly, small search length was used (10^{-7}), resulting in a moderate number of iterations. For the examples reported herein, the search length can be reduced significantly (2 orders of magnitude) without affecting the quality of the converged profiles. The number of iterations can be further reduced by increasing the sampling frequency points in the target band gap.

6. Conclusions

We discussed an approach for the inverse design of metamaterials, driven by a user-defined band gap. To this end, we showed that the sign of the discriminant of the associated quadratic eigenvalue problem serves as a sharp indicator of propagating and evanescent states. Then, we formulated an inverse medium problem using the discriminant as the driving objective functional, and the associated eigenvalue problem as a side constraint. We demonstrated the performance of the inversion method with various numerical examples in one and two dimensions using scalar waves.

In summary, we conclude:

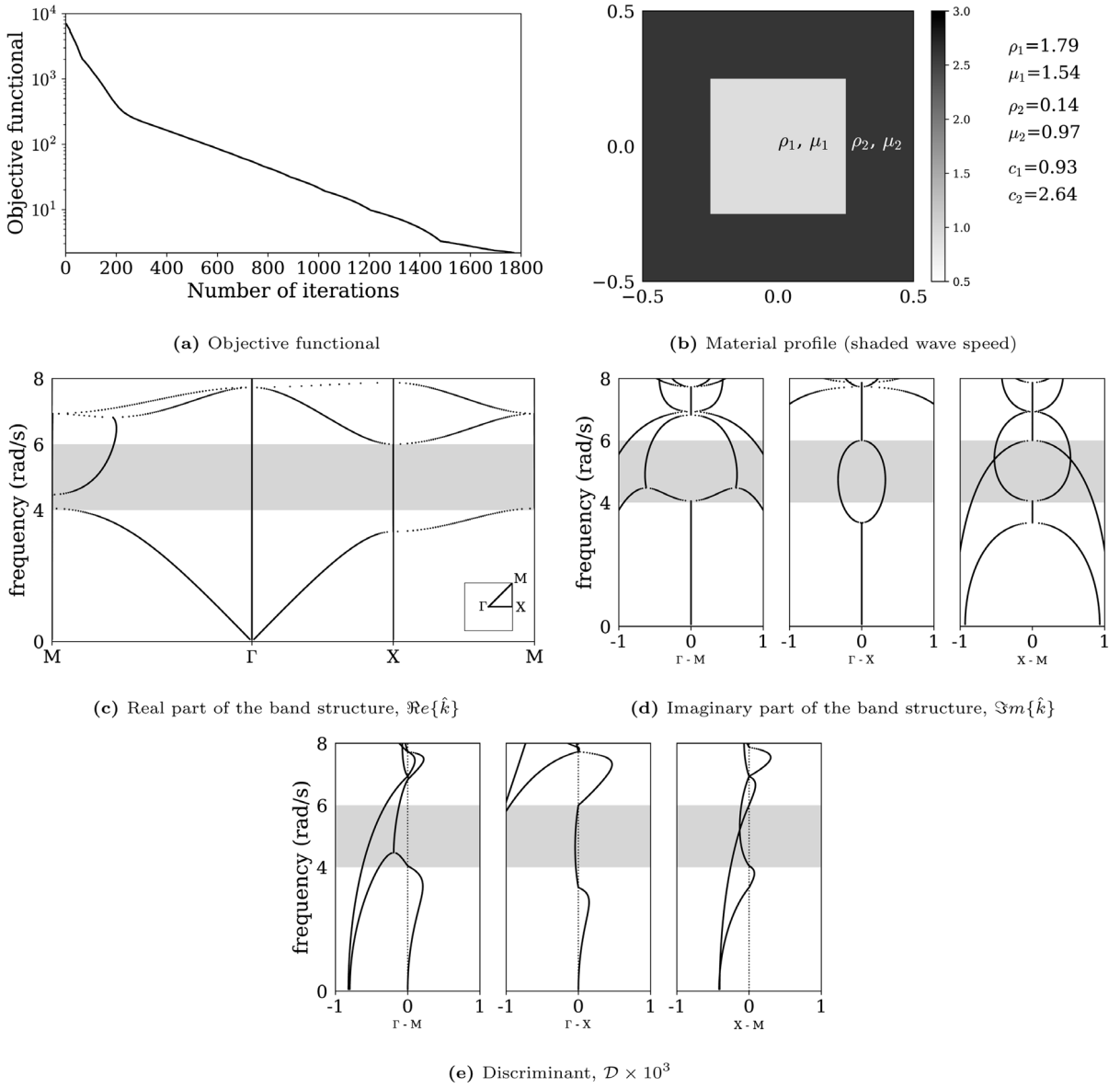

(a) Objective functional

(b) Material profile (shaded wave speed)

(c) Real part of the band structure, $\Re e\{\hat{k}\}$

(d) Imaginary part of the band structure, $\Im m\{\hat{k}\}$

(e) Discriminant, $\mathcal{D} \times 10^3$

Fig. 19. Inversion for 2 materials elements for an omni-directional band gap at 4–6 rad/s; band gap shown shaded.

- The discriminant uniquely identifies propagating and evanescent states, and, thus, forms an ideal basis for band-gap design;
- The proposed discriminant-based objective functional does not require prior knowledge of the exact band structure;
- The proposed discriminant-based objective functional is differentiable, which is necessary for gradient-based optimization algorithms;
- The inversion process is capable of designing band-gap materials with various target band gaps; and
- The inverted band-gap materials can be used in metamaterials to attenuate incoming waves at the band-gap frequencies.

Acknowledgments

Partial support for the first author was provided by a University of Texas at Austin VPR Research Grant; the support is gratefully acknowledged. We also wish to thank Professor Andrea Alù for fruitful discussions, as well as the anonymous reviewers and the editors for their constructive comments.

Appendix. Gâteaux derivatives of L

The 1st-order Gâteaux derivative with respect to u of F, or $\delta_u F[u](\tilde{u})$, is defined as

$$\delta_u F[u](\tilde{u}) = \left.\frac{d}{d\varepsilon}\right|_{\varepsilon=0} F[u+\varepsilon\tilde{u}], \tag{A.1}$$

where $\tilde{u}$ is the direction of the Gâteaux derivative. The Fréchet derivative g_u is defined as [25]

$$\int_\Omega \tilde{u} g_u d\Omega = \delta_u F[u](\tilde{u}). \tag{A.2}$$

The (Gâteaux) derivatives of the Lagrangian L are given below; to reduce the notational congestion, we replace $[\rho, \mu, u, k, v, \xi]$ with $[\ldots]$.

The derivatives with respect to the adjoint variables are:

$$\delta_{v_0^{(i)}} L[\ldots]\left(\tilde{v}_0^{(i)}\right) = \Re e\left\{P\left(k_0^{(i)}\right)\left(\tilde{v}_0^{(i)}, u_0^{(i)}\right)\right\} \text{ and} \tag{A.3}$$

$$\delta_{\xi_0^{(i)}} L[\ldots]\left(\tilde{\xi}_0^{(i)}\right) = \frac{\tilde{\xi}_0^{(i)}}{2}\left[a_2\left(u_0^{(i)}, u_0^{(i)}\right) - 1\right] = \Re e\left\{\frac{\tilde{\xi}_0^{(i)}}{2}\left[a_2\left(u_0^{(i)}, u_0^{(i)}\right) - 1\right]\right\}. \tag{A.4}$$

The derivatives with respect to the state variables are:

$$\delta_{u_0^{(i)}} L[\ldots]\left(\tilde{u}_0^{(i)}\right) = \delta_{u_0^{(i)}} D[\ldots]\left(\tilde{u}_0^{(i)}\right) + \delta_{u_0^{(i)}} E[\ldots]\left(\tilde{u}_0^{(i)}\right) \text{ and} \tag{A.5}$$

$$\delta_{k_0^{(i)}} L[\ldots]\left(\tilde{k}_0^{(i)}\right) = \delta_{k_0^{(i)}} D[\ldots]\left(\tilde{k}_0^{(i)}\right) + \delta_{k_0^{(i)}} E[\ldots]\left(\tilde{k}_0^{(i)}\right), \tag{A.6}$$

where

$$\begin{aligned}\delta_{u_0^{(i)}} D[\ldots]\left(\tilde{u}_0^{(i)}\right) &= 4a_1\left(u_0^{(i)}, u_0^{(i)}\right)\Re e\left\{a_1\left(u_0^{(i)}, \tilde{u}_0^{(i)}\right)\right\} - 8a_2\left(u_0^{(i)}, u_0^{(i)}\right)\Re e\left\{a_0\left(u_0^{(i)}, \tilde{u}_0^{(i)}\right)\right\} \\ &\quad - 8a_0\left(u_0^{(i)}, u_0^{(i)}\right)\Re e\left\{a_2\left(u_0^{(i)}, \tilde{u}_0^{(i)}\right)\right\} \\ &= \Re e\left\{4a_1\left(u_0^{(i)}, u_0^{(i)}\right)a_1\left(u_0^{(i)}, \tilde{u}_0^{(i)}\right)\right\} - \Re e\left\{8a_2\left(u_0^{(i)}, u_0^{(i)}\right)a_0\left(u_0^{(i)}, \tilde{u}_0^{(i)}\right)\right\} \\ &\quad - \Re e\left\{8a_0\left(u_0^{(i)}, u_0^{(i)}\right)a_2\left(u_0^{(i)}, \tilde{u}_0^{(i)}\right)\right\},\end{aligned} \tag{A.7}$$

$$\delta_{u_0^{(i)}} E[\ldots]\left(\tilde{u}_0^{(i)}\right) = \Re e\left\{P\left(k_0^{(i)}\right)\left(v_0^{(i)}, \tilde{u}_0^{(i)}\right)\right\} + \Re e\left\{\xi_0^{(i)} a_2\left(u_0^{(i)}, \tilde{u}_0^{(i)}\right)\right\}, \tag{A.8}$$

$$\delta_{k_0^{(i)}} D[\ldots]\left(\tilde{k}_0^{(i)}\right) = 0, \text{ and} \tag{A.9}$$

$$\delta_{k_0^{(i)}} E[\ldots]\left(\tilde{k}_0^{(i)}\right) = \Re e\left\{\tilde{k}_0^{(i)} a_1\left(v_0^{(i)}, u_0^{(i)}\right) + 2k_0^{(i)}\tilde{k}_0^{(i)} a_2\left(v_0^{(i)}, u_0^{(i)}\right)\right\}. \tag{A.10}$$

The derivatives with respect to the design variables (ρ and μ) are:

$$\delta_\rho L[\ldots](\tilde{\rho}) = \delta_\rho D[\ldots](\tilde{\rho}) + \delta_\rho E[\ldots](\tilde{\rho}) \text{ and} \tag{A.11}$$

$$\delta_\mu L[\ldots](\tilde{\mu}) = \delta_\mu D[\ldots](\tilde{\mu}) + \delta_\mu E[\ldots](\tilde{\mu}), \tag{A.12}$$

where

$$\delta_\rho D[\ldots](\tilde{\rho}) = -\sum_i^N 4a_2\left(u_0^{(i)}, u_0^{(i)}\right)\delta_\rho a_0\left(u_0^{(i)}, u_0^{(i)}\right) = \sum_i^N \Re e\left\{4a_2\left(u_0^{(i)}, u_0^{(i)}\right)\int_0^p \overline{u}^{(i)}\omega^2\tilde{\rho}\, u_0^{(i)} dx\right\}, \tag{A.13}$$

$$\delta_\rho E[\ldots](\tilde{\rho}) = \sum_i^N \delta_\rho \Re e\left\{a_0\left(v_0^{(i)}, u_0^{(i)}\right)\right\} = -\sum_i^N \Re e\left\{\int_0^p \overline{v}^{(i)}\omega^2\tilde{\rho}\, u_0^{(i)} dx\right\}, \tag{A.14}$$

$$\begin{aligned}\delta_\mu D[\ldots](\tilde{\mu}) &= \sum_i^N 2a_1\left(u_0^{(i)}, u_0^{(i)}\right)\delta_\mu a_1\left(u_0^{(i)}, u_0^{(i)}\right) - \sum_i^N 4a_2\left(u_0^{(i)}, u_0^{(i)}\right)\delta_\mu a_0\left(u_0^{(i)}, u_0^{(i)}\right) \\ &\quad - \sum_i^N 4a_0\left(u_0^{(i)}, u_0^{(i)}\right)\delta_\mu a_2\left(u_0^{(i)}, u_0^{(i)}\right) \\ &= \sum_i^N \Re e\left\{2a_1\left(u_0^{(i)}, u_0^{(i)}\right)\int_0^p \mathrm{i}\left(\frac{\partial\overline{u}^{(i)}}{\partial x}\tilde{\mu}\, u_0^{(i)} - \overline{u}^{(i)}\tilde{\mu}\frac{\partial u_0^{(i)}}{\partial x}\right)dx\right\}\end{aligned}$$

$$- \sum_i^N \Re e \left\{ 4a_2 \left(u_0^{(i)}, u_0^{(i)} \right) \int_0^p \frac{\partial \overline{u}^{(i)}}{\partial x} \tilde{\mu} \frac{\partial u_0^{(i)}}{\partial x} dx \right\}$$

$$- \sum_i^N \Re e \left\{ 4a_0 \left(u_0^{(i)}, u_0^{(i)} \right) \int_0^p \overline{u}^{(i)} \tilde{\mu}\, u_0^{(i)} dx \right\}, \text{ and} \tag{A.15}$$

$$\delta_\mu E[\ldots](\tilde{\mu}) = \sum_i^N \delta_\mu \Re e \left\{ P\left(k_0^{(i)}\right) \left(v_0^{(i)}, u_0^{(i)} \right) \right\} + \sum_i^N \frac{\xi_0^{(i)}}{2} \delta_\mu a_2 \left(u_0^{(i)}, u_0^{(i)} \right)$$

$$= \sum_i^N \Re e \left\{ k_0^{(i)} \int_0^p \mathrm{i} \left(\frac{\partial \overline{v}^{(i)}}{\partial x} \tilde{\mu}\, u_0^{(i)} - \overline{v}^{(i)} \tilde{\mu} \frac{\partial u_0^{(i)}}{\partial x} \right) dx \right\} + \sum_i^N \Re e \left\{ \int_0^p \frac{\partial \overline{v}^{(i)}}{\partial x} \tilde{\mu} \frac{\partial u_0^{(i)}}{\partial x} dx \right\}$$

$$+ \sum_i^N \Re e \left\{ \left(k_0^{(i)}\right)^2 \int_0^p \overline{v}^{(i)} \tilde{\mu}\, u_0^{(i)} dx \right\} + \sum_i^N \Re e \left\{ \frac{\xi_0^{(i)}}{2} \int_0^p \overline{u}^{(i)} \tilde{\mu}\, u_0^{(i)} dx \right\}. \tag{A.16}$$

References

[1] C. Kittel, Introduction to Solid State Physics, Wiley, 2005.
[2] J.B. Pendry, Negative refraction makes a perfect lens, Phys. Rev. Lett. 85 (2000) 3966–3969, http://dx.doi.org/10.1103/PhysRevLett.85.3966.
[3] C. Luo, S.G. Johnson, J.D. Joannopoulos, J.B. Pendry, Subwavelength imaging in photonic crystals, Phys. Rev. B 68 (2003) 045115, http://dx.doi.org/10.1103/PhysRevB.68.045115.
[4] N.W. Ashcroft, Solid State Physics, Holt, Rinehart and Winston, 1976, p. 403.
[5] M.S. Kushwaha, P. Halevi, L. Dobrzynski, B. Djafari-Rouhani, Acoustic band structure of periodic elastic composites, Phys. Rev. Lett. 71 (1993) 2022–2025, http://dx.doi.org/10.1103/PhysRevLett.71.2022.
[6] F.R. Montero de Espinosa, E. Jiménez, M. Torres, Ultrasonic band gap in a periodic two-dimensional composite, Phys. Rev. Lett. 80 (1998) 1208–1211, http://dx.doi.org/10.1103/PhysRevLett.80.1208.
[7] L. Brillouin, Wave Propagation in Periodic Structures: Electric Filters and Crystal Lattices, McGraw-Hill Book Company, Inc., 1946.
[8] O. Sigmund, J. Søndergaard Jensen, Systematic design of phononic band–gap materials and structures by topology optimization, Philos. Trans. R. Soc. Lond. Ser. A Math. Phys. Eng. Sci. 361 (1806) (2003) 1001–1019, http://dx.doi.org/10.1098/rsta.2003.1177.
[9] C.J. Rupp, A. Evgrafov, K. Maute, M.L. Dunn, Design of phononic materials/structures for surface wave devices using topology optimization, Struct. Multidiscip. Optim. 34 (2) (2007) 111–121, http://dx.doi.org/10.1007/s00158-006-0076-0.
[10] X. Qian, O. Sigmund, Isogeometric shape optimization of photonic crystals via coons patches, Comput. Methods Appl. Mech. Engrg. 200 (25) (2011) 2237–2255, http://dx.doi.org/10.1016/j.cma.2011.03.007.
[11] Y. Wang, Z. Luo, N. Zhang, Z. Kang, Topological shape optimization of microstructural metamaterials using a level set method, Comput. Mater. Sci. 87 (2014) 178–186, http://dx.doi.org/10.1016/j.commatsci.2014.02.006.
[12] H. Sadeghi, S. Nemat-Nasser, Design optimization of layered periodic composites for desired elastodynamic response, in: T. Kundu (Ed.), in: Proc. SPIE, Health Monitoring of Structural and Biological Systems, vol. 9438, 2015, pp. 94380T1– 94380T8, http://dx.doi.org/10.1117/12.2083048.
[13] L.F. Kallivokas, A. Fathi, S. Kucukcoban, K.H. Stokoe, J. Bielak, O. Ghattas, Site characterization using full waveform inversion, Soil Dyn. Earthq. Eng. 47 (2013) 62–82, http://dx.doi.org/10.1016/j.soildyn.2012.12.012.
[14] A. Fathi, L.F. Kallivokas, B. Poursartip, Full-waveform inversion in three-dimensional pml-truncated elastic media, Comput. Methods Appl. Mech. Engrg. 296 (2015) 39–72, http://dx.doi.org/10.1016/j.cma.2015.07.008.
[15] M.S. Kushwaha, P. Halevi, L. Dobrzynski, B. Djafari-Rouhani, Acoustic band structure of periodic elastic composites, Phys. Rev. Lett. 71 (1993) 2022–2025, http://dx.doi.org/10.1103/PhysRevLett.71.2022.
[16] M.I. Hussein, M.J. Leamy, M. Ruzzene, Dynamics of phononic materials and structures: Historical origins, recent progress, and future outlook, Appl. Mech. Rev. 66 (4) (2014) 040802–1–040802–38, http://dx.doi.org/10.1115/1.4026911.
[17] B. Banerjee, An Introduction to Metamaterials and Waves in Composites, CRC Press, 2011.
[18] V. Akçelik, G. Biros, O. Ghattas, D. Keyes, K. Ko, L. Lee, E.G. Ng, Adjoint methods for electromagnetic shape optimization of the low-loss cavity for the international linear collider, J. Phys. Conf. Ser. 16 (1) (2005) 435, http://dx.doi.org/10.1088/1742-6596/16/1/059.
[19] H. Mashayekh, L.F. Kallivokas, J.L. Tassoulas, Parameter estimation in layered media using dispersion-constrained inversion, J. Eng. Mech. 144 (2018) 04018099, http://dx.doi.org/10.1061/(ASCE)EM.1943-7889.0001527.
[20] A. Quarteroni, R. Sacco, F. Saleri, Numerical Mathematics, Vol. 37, Springer Science & Business Media, 2010, http://dx.doi.org/10.1007/b98885.
[21] R. Fletcher, C.M. Reeves, Function minimization by conjugate gradients, Comput. J. 7 (2) (1964) 149–154, http://dx.doi.org/10.1093/comjnl/7.2.149.
[22] S. Balay, S. Abhyankar, M.F. Adams, J. Brown, P. Brune, K. Buschelman, L. Dalcin, V. Eijkhout, W.D. Gropp, D. Kaushik, M.G. Knepley, L.C. McInnes, K. Rupp, B.F. Smith, S. Zampini, H. Zhang, H. Zhang, PETSc Users Manual, Tech. Rep. ANL-95/11 - Revision 3.7, Argonne National Laboratory, 2016.
[23] J.E. Roman, C. Campos, E. Romero, A. Tomas, SLEPc Users Manual, Tech. Rep. DSIC-II/24/02 - Revision 3.7, D. Sistemes Informàtics i Computació, Universitat Politècnica de València, 2016.
[24] C. Campos, J.E. Roman, Parallel Krylov solvers for the polynomial eigenvalue problem in SLEPc, SIAM J. Sci. Comput. (2016) http://dx.doi.org/10.1137/15M1022458.
[25] M. Stone, P. Goldbart, Mathematics for Physics: A Guided Tour for Graduate Students, Cambridge University Press, 2009.